


2019-01-01

Microstructure Evolution Of Chalcogenide Materials Via Molecular Dynamics

Sharmin Abdullah

University of Texas at El Paso, sharmin03abdullah@gmail.com

Follow this and additional works at: https://digitalcommons.utep.edu/open_etd

 Part of the [Electrical and Electronics Commons](#), [Materials Science and Engineering Commons](#), and the [Mechanics of Materials Commons](#)

Recommended Citation

Abdullah, Sharmin, "Microstructure Evolution Of Chalcogenide Materials Via Molecular Dynamics" (2019). *Open Access Theses & Dissertations*. 1966.

https://digitalcommons.utep.edu/open_etd/1966

This is brought to you for free and open access by DigitalCommons@UTEP. It has been accepted for inclusion in Open Access Theses & Dissertations by an authorized administrator of DigitalCommons@UTEP. For more information, please contact lweber@utep.edu.

MICROSTRUCTURE EVOLUTION OF CHALCOGENIDE MATERIALS VIA
MOLECULAR DYNAMICS

SHARMIN ABDULLAH

Master's Program in Computational Science

APPROVED:

David Zubia, Ph.D., Chair

Xiaowang Zhou, Ph.D.

Michael Pokojovy, Ph.D.

Stephen Crites, Ph.D.
Dean of the Graduate School

Copyright ©

by

Sharmin Abdullah

2019

Dedication

To my family, instructors and friends

MICROSTRUCTURE EVOLUTION OF CHALCOGENIDE MATERIALS VIA MOLECULAR DYNAMICS

by

SHARMIN ABDULLAH, BS

THESIS

Presented to the Faculty of the Graduate School of

The University of Texas at El Paso

in Partial Fulfillment

of the Requirements

for the Degree of

MASTER OF SCIENCE

Computational Science Program

THE UNIVERSITY OF TEXAS AT EL PASO

May 2019

Acknowledgements

I would first like to thank my advisor Dr. David Zubia for the continuous support and encouragement in my study and thesis. His guidance and immense knowledge have always helped me to give my best effort and be successful in my work. I would also like to thank the rest of my thesis committee: Dr. Xiaowang Zhou and Dr. Michael Pokojovy, for their encouragement, insightful comments, and questions. Moreover, this thesis would not have been possible without the constant support, mentorship and guidance of Dr. Rodolfo Aguirre and the computational data from Dr. Xiaowang Zhou.

I would like to thank my father, A. K. M. Abdullah and mother, Bilkis Akhter for always supporting me and encouraging me to achieve my goals. I thank my husband, Tahsin Rahman for his tremendous care and support, and always giving me encouragement for anything I needed.

I thank Khodeza Begum for helping me and treating me as family and Asad Ullah Hil Gulib and M Masum Bhuiyan for being magnificent friends and classmates. I would like to thank my uncles, aunts and cousins who care about me and my education.

In conclusion, I would like to express my sincere thanks to my program director Dr. Ming-Ying Leung for always helping me with academic guidance and encouraging me to do better with my work.

Abstract

The properties of a material are defined by its granular microstructure which is determined by its grain evolution and the types of grain boundaries present in the structure. For example, the performance of Cadmium Sulfide/Cadmium Telluride (CdS/CdTe) solar cells can be affected by the presence of grain boundaries which makes the study of grain structure evolution a very important part of solar cell performance optimization. Grain boundary mobilities are important properties in material science and engineering as they determine grain structures under given processing and operating conditions.

In this thesis, several computational tools were used to analyze the formation and behavior of grains and grain boundaries in poly-crystalline CdTe/CdS and bi-crystalline CdTe structures. Recently, the simulated growth of a polycrystalline CdTe/CdS structure via molecular dynamics was reported which very closely mimics the experimental structure of these materials. However, a detailed analysis of the grain boundaries in the simulated CdTe/CdS is lacking. The goal of this thesis is to develop a general methodology to quantitatively analyze the behavior of the grain boundaries in the CdTe/CdS structure. Orientation of the grains within the polycrystalline CdTe/CdS was successfully computed using a combination of computational tools. The determination of the orientation of neighboring grains in a polycrystalline sample is important for computing the type of grain boundaries within the structure. Moreover, the migration of $\Sigma 3(111)$, $\Sigma 7(111)$ and $\Sigma 11(311)$ grain boundaries in CdTe bi-crystals at various temperatures and one driving forces was also computed. The grain boundary migration study is important to calculate the mobility of the grain boundary. Future work will focus on computing the grain boundary types in the polycrystalline sample and studying their dynamic behavior.

Table of Contents

Dedication	iii
Acknowledgements	v
Abstract	vi
Table of Contents	vii
List of Figures	ix
Chapter 1: Introduction & Motivation	1
1.1 Overview	1
1.2 History of CdTe Solar cell	1
1.3 Problem Statement	3
1.4 Contribution of this Thesis	5
Chapter 2: Technical Background	6
2.1 Type of Grain Boundaries in CdTe	6
2.2 Molecular Dynamics	11
2.2.1 Interatomic Potential	11
2.2.2 Newton's Law of Particle Motions	12
2.2.3 LAMMPS	13
Chapter 3: Methodologies	14
3.1 Computer Resources	14
3.2 Conditions for Poly-Crystalline Growth	14
3.3 Creation of CdTe Bi-Crystals	17
3.4 Algorithm for Boundary Migration	18
3.5 Configuration for Boundary Migration in CdTe Bi-Crystals	18
3.6 Grain Structure and Grain Boundary Analysis	20
3.7 Grain Orientation Analysis	20
Chapter 4: Results	24
4.1 Analysis of CdTe/CdS Polycrystalline Growth	24
4.2 Analysis of Crystal Orientation	28
4.2.1 Validation of GTA Grain Orientation Tool	28
4.2.2 Texture Analysis of Polycrystalline CdTe/CdS Sample	29

4.3 Analysis of Grain Boundary Migration in CdTe Bi-Crystals	31
Chapter 5: Future Work	35
5.1 Research Goal	35
5.2 Timeline	38
References	40
Appendices.....	42
Appendix A- Input file for Creating $\Sigma 3(111)$ using LAMMPS code	42
Appendix B- Input file for Creating $\Sigma 7(111)$	45
Appendix C- Input file for Creating $\Sigma 11(311)$	47
Appendix D- Code for executing $\Sigma 7(111)$ Boundary Migration	50
Appendix E- Modified MATLAB code to run GTA Tool	52
Vita	53

List of Figures

Figure 1: Best solar cell efficiencies [7].	3
Figure 2. (a) A tilt boundary and (b) A twist boundary[20].	6
Figure 3: (100) Simple Cubic Lattice	7
Figure 4: 3D EBSD reconstruction of CdTe layer. (a) Colored grains for the crystallographic orientation, (b) grain boundaries colored according to the disorientation angle, (c) only random high angle grain boundary network, (d) $\Sigma 3$ twin boundary, (e) inverse pole figure[22].	9
Figure 5: Grain boundary map of a CdTe film via electron back-scatter diffraction (EBSD) [9].	10
Figure 6: CdTe/CdS heterostructure grown by CdTe deposition on CdS layer.	15
Figure 7. (a) Single crystal CdS layer and (b) amorphous CdS after melting phase.	16
Figure 8. (a) Atomic and (b) structure maps of the initial stages of growth of CdS on the amorphous layer.	17
Figure 9. Grain boundary structure of (a) $\Sigma 3(111)$, (b) $\Sigma 3(111)$ and (c) $\Sigma 3(111)$.	18
Figure 10. Grain boundary migration configuration of $\Sigma 11$	19
Figure 11. (a) Visualization of polycrystalline Te atomistic structure with the [010] simulation direction, (b) inverse pole figure representing crystal orientation.	21
Figure 12. Displacement vector calculation for FCC. [38]	22
Figure 13. Top view of the CdS structure at thicknesses (times) of (a) 2.1 nm (2 ns), (b) 3.6 nm (12 ns), and (c) 10 nm (48 ns).	25
Figure 14: Top view of the CdTe growth at sample thickness (times) of (a) 10.2 nm (48.4 ns) (b) 11.1 nm (56.4 ns), (c) 11.5 nm (58.4 ns), and (d) 14.1 nm (68.4 ns).	27
Figure 15. Slices of CdTe/CdS heterostructure at 68.4 ns.	28
Figure 16. Crystal orientation of $\Sigma 7(111)$ visualized by (a) Ovito, (b) GTA grain orientation, (c) Inverse pole figure, d) positive pole figure in [001] direction.	29
Figure 17. (a) Crystal structure visualized by OVITO, (b) Crystal orientation by GTA.	30
Figure 18: Validation of GTA output through comparison of visualization method (a) Ovito output, (b) GTA output.	30
Figure 19. Grain boundary migration of (a) $\Sigma 3(111)$, (b) $\Sigma 7(111)$, (c) $\Sigma 11(311)$ grain boundaries at 1800 K and added energy of 1 eV.	32
Figure 20. Grain boundary migration mechanism of $\Sigma 11(311)$ at 1000 K and added energy of 1 eV.	33
Figure 21. Graphical representation of grain boundary motion of $\Sigma 3(111)$, $\Sigma 7(111)$ and $\Sigma 11(311)$ (a) at 1200 K and (b) at 1800 K.	34
Figure 22. Block diagram of the proposed work	36
Figure 23. Sample of orientation data from GTA	36
Figure 24. Timeline for the Proposed Work	39

Chapter 1: Introduction & Motivation

1.1 OVERVIEW

Elements from group II and group VI from the periodic table form good semiconductor compounds (chalcogenide) for optical applications. For example, Cadmium Telluride (CdTe) is popular for its use in photovoltaics and x-ray detectors. Specifically, the thin-film photovoltaic chalcogenide CdTe is very promising to produce sustainable and environment friendly electricity from sunlight [1]. Also, the manufacturing cost of CdTe solar cells is lower than silicon [2]. Moreover, CdTe is a direct bandgap semiconductor which yields a high absorption coefficient ($>10^4 \text{ cm}^{-1}$) [3] which makes it suitable for optoelectronic applications. Finally, it has an energy bandgap of 1.5 electron volts (eV) [4] which is optimum for photovoltaic conversion.

1.2 HISTORY OF CdTe SOLAR CELL

CdTe solar cells convert the energy of light into electricity very efficiently due to its high optical absorption coefficient [5] and ideal band gap (1.5 eV). Additionally, CdTe thin film solar cells have a competitive module cost in the market ($\sim 45\text{¢/W}$), making them a desirable thin film technology. However, practically, the solar cell efficiency is below the Shockley-Queisser efficiency limit. To increase competitiveness compared to fossil fuels, increasing the solar conversion efficiency in CdTe modules from 22% to 28% is critical. Figure 1 shows the improvement of solar cell efficiency for several materials systems over the years from 1975 to present day. For CdTe in particular, the 1980's saw the identification of a stable CdTe/CdS junction. Major breakthroughs in the 1990's were; the maximization of the short-circuit current, J_{SC} , to 26 mA/cm^2 through thinning of the CdS layer and incorporation of a high-resistivity buffer layer; and development of a CdCl_2 treatment that passivated defects to achieve fill-factors of 76%,

and open-circuit voltages of 0.85 V. This was accomplished mainly by Photon Energy Inc (an El Paso based company) and the University of South Florida. In the 2000's, a stable contact to CdTe was developed mainly by the work of Colorado State University which provided a stable cell, and mass production began but no great improvement in efficiency was achieved. In the 2010's, First Solar Inc demonstrated significant efficiency improvement mainly by increases in the open-circuit voltage and fill-factor. Out all of these advancements, the open-circuit voltage continues to have the most room for further improvement.

The polycrystalline nature, lattice mismatch, and other crystal growth phenomena of CdTe and CdS materials cause defects that reduce the open-circuit voltage. Defects trap carriers and reduce the voltage, fill-factor (FF) and efficiency of CdTe PV modules. Moreover, spatial non-uniformity of grains in polycrystalline films creates lossesⁱ and interdependencies between various device components and this has compelled a predominantly empirical development of the device. Recent enhancements on material quality at the atomic scale have increased the solar cell efficiency up to 22.1% and have confirmed new pathways to increase CdTe solar cell efficiency to theoretical values. Its theoretical efficiency limit is ~30% [6], therefore there is still a 7.9% room for improvement.

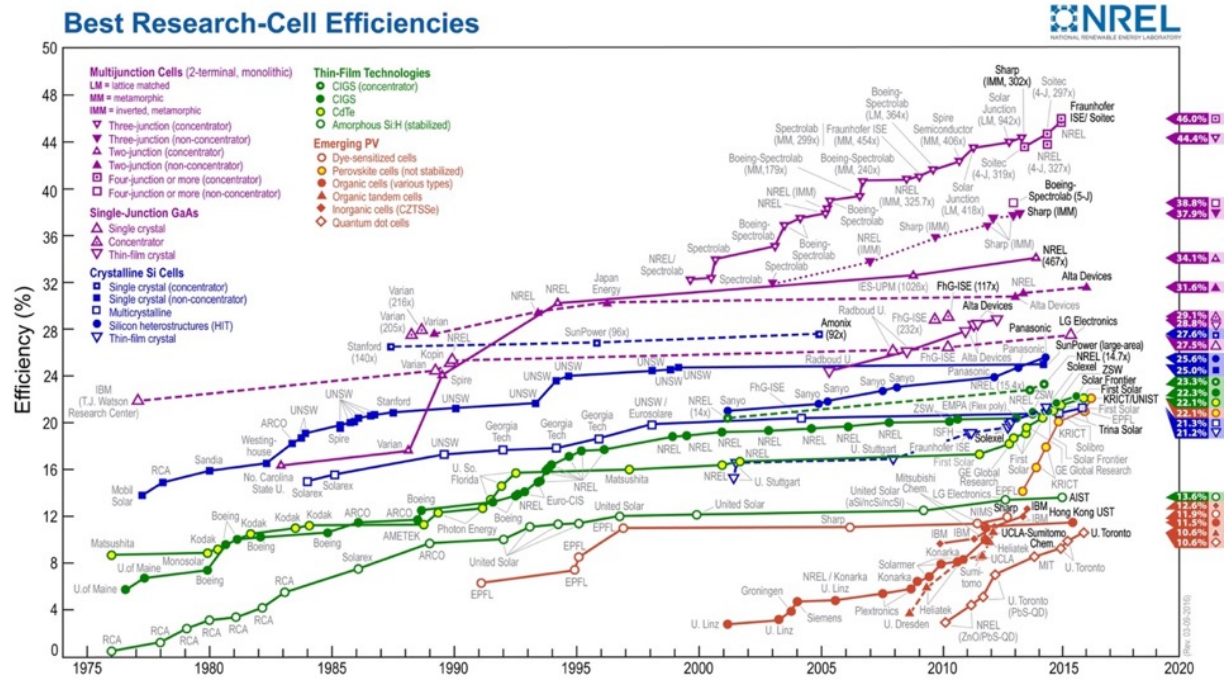


Figure 1: Best solar cell efficiencies [7].

1.3 PROBLEM STATEMENT

In order to achieve efficiencies above 22.1%, the open circuit voltage (V_{OC}) needs to be increased [8]. V_{OC} depends on the saturation current and the saturation current is affected by carrier recombination and concentration. Carrier recombination occurs at defects such as grain boundaries [9]. However, the structure and evolution of these grain boundaries is not fully understood. Therefore, to increase the V_{OC} , a deeper understanding of grain boundary structures and their evolution in the poly-crystalline CdTe/CdS layer stack is required. The physical, chemical, mechanical and electronic properties of the material is strongly influenced by its granular microstructure which is determined by its grain evolution and the types of grain boundaries [10] present in the structure.

From experimental studies it has been seen that the microstructure and quality of a heteroepitaxial film is greatly impacted by the surface orientation and termination of the substrate. However, the techniques used to obtain this high-resolution structural result are incomplete, destructive, expensive or time consuming. For example, scanning transmission electron microscopy (STEM) [11] is effective at revealing two-dimensional (2-D) microstructures with atomic resolution, but cannot provide three-dimensional (3-D) information that determines material properties and defect evolution. Atomic probe tomography [12] provides rich 3-D compositional information, but is unable to resolve lattice and defect structure with atomic resolution. On the other hand, atomistic simulations such as molecular dynamics (MD) [13], [14] allow virtual experiments that isolate external factors, offer a 3-D analysis of the heteroepitaxial microstructures and can rapidly generate a large database of atomic scale structures of films as a function of substrate characteristics including all commonly encountered substrate orientations. Creating a similar database from experiments alone is highly prohibitive.

Using MD simulations, Rodolfo Aguirre et al. [15] developed a methodology to simulate the growth of polycrystalline CdTe/CdS heterostructures that very closely mimic experimental structures without any assumptions regarding the microstructure. They found defects such as grain boundaries at the CdTe/CdS interface. Their crystal phase analysis showed that zinc blende structure dominates over the wurtzite structure inside both CdS and CdTe grains. Moreover, grain boundary migration during the early stage growth of CdTe was also observed.

Several computational materials scientists have recently started working to develop tools for quantifying structure in atomistic simulations. For example, Xu and Li [16] developed a technique for identifying atoms that are part of grain boundaries, triple junctions, and vertices. In addition, a dislocation extraction algorithm (DXA) that can identify crystal structures, grain

boundaries, and dislocations has been created by Stukowski et al [17]. Other authors have developed techniques to characterize microstructure. For example, Tucker and Foiles [18] developed a technique for finding individual grains within a polycrystalline sample, allowing for quantitative measurements of grain size. Recently, Panzarino et al [19] developed a post-processing tool that identifies crystalline grains and precisely calculates grain orientations with no prior knowledge of the simulated fcc and bcc microstructure. However, other structures such as zincblende and wurtzite still cannot be simulated with any tool. Moreover, the type of grain boundary in between the grains for all types of crystal structures for example zincblend, wurtzite, FCC together cannot be identified directly with the tools presently available.

1.4 CONTRIBUTION OF THIS THESIS

This thesis analyzes the simulated growth of a polycrystalline CdTe/CdS bilayer and the migration of grain boundaries in predefined CdTe bi-crystals. The polycrystalline CdTe/CdS bilayer was previously created via molecular dynamics (MD) simulations. This thesis focused on observing early-stage crystallite nucleation, grain and grain-boundary formation, and grain growth phenomena. Another contribution is the analysis of the orientation of the grains and location of grain boundaries within the polycrystalline structures at various stages of growth.

This thesis also studied migration of grain boundaries in predefined CdTe bi-crystal structures. In particular the motion of $\Sigma 3$, $\Sigma 7$ and $\Sigma 11$ grain boundaries to quantify their mobilities were analyzed. An atomic scale mechanism for the motion of $\Sigma 11$ grain boundaries is proposed. Overall, this work will allow the development of better predictive simulations of grain structure evolution which will provide valuable insights into making better quality materials for solar cells.

Chapter 2: Technical Background

2.1 TYPE OF GRAIN BOUNDARIES IN CdTe

There are different types of grain boundaries depending on the grain or crystal orientation rotation. The grain boundary can be best depicted by representing the rotation in terms of an axis and angle of rotation. If the rotation axis is parallel to the grain boundary plane then it is called a tilt boundary as shown in Figure 2(a). On the other hand, the boundary is called a twist boundary if the rotation axis is perpendicular to the grain boundary plane as shown in Figure 2(b). If the adjacent crystals are mirror images of each other, then the grain boundary is referred to as a symmetric tilt boundary. All other tilt boundaries are called asymmetric tilt boundaries.

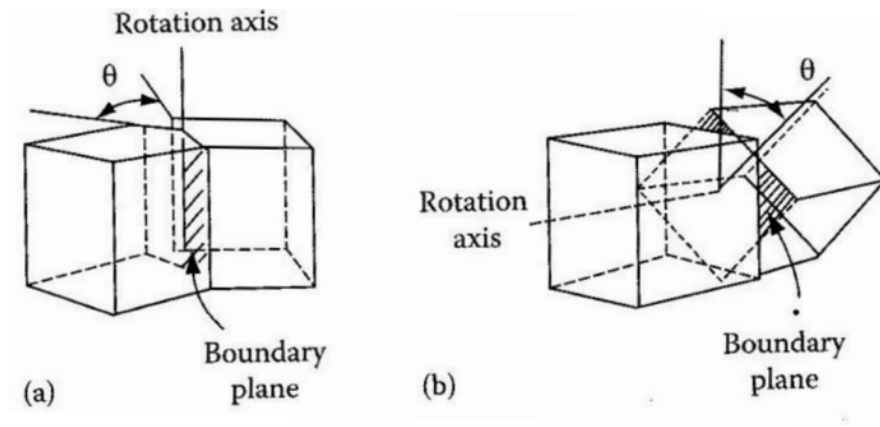


Figure 2. (a) A tilt boundary and (b) A twist boundary[20].

With respect to the misorientation between the adjacent grains, there are two types of grain boundaries; low-angle and high-angle grain boundaries. The boundary is called low-angle if the misorientation between the adjacent grains is small and the boundary is entirely comprised of a periodic crystal dislocation arrangement. For rotation angles larger than 15° , the dislocations lose their identity as individual lattice defects. Therefore, grain boundaries with rotation angles in

excess of 15° are distinguished from the low-angle grain boundaries and are termed high-angle grain boundaries.

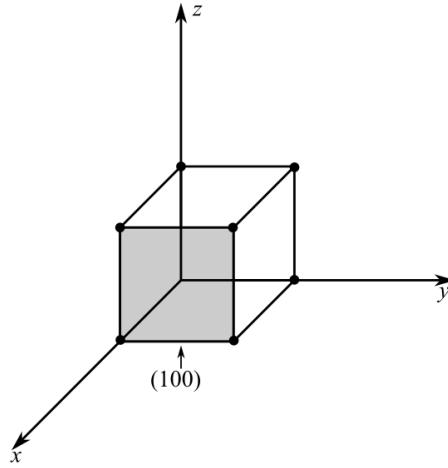


Figure 3: (100) Simple Cubic Lattice.

If the atomic positions of both adjacent lattices in a (100) grain boundary plane are considered, then the occurrence of many coincidence sites is evident. Since both crystal lattices are periodic, the coincidence sites also must be periodic, i.e. they also define a lattice called the coincidence site lattice (CSL). The elementary cell of the CSL is larger than the elementary cell of the crystal lattice. As a measure for the density of coincidence sites or for the size of the elementary cell of the CSL, the quantity is defined,

$$\Sigma = \frac{\text{volume elementary cell of CSL}}{\text{volume elementary cell of crystal lattice}} \quad (1)$$

For example, For the rotation 36.87° $\langle 100 \rangle$ is $\Sigma = \frac{a(a\sqrt{5})^2}{a^3} = 5$ where a is the lattice parameter [21].

Experimentally, researchers have studied grain orientation and grain boundaries in CdTe films using electron-backscattered diffraction (EBSD). In EBSD, electrons that are backscattered from a smooth material surface (when exposed to an incident electron beam in a scanning electron microscope) contain crystallographic orientation information of the grains. This information is captured by a camera and analyzed by a computer to create colored 2-dimensional maps of the grain orientation and grain boundaries of the material surface. To obtain 3-dimensional information, thin layers of the material are milled using an ion beam and successive 2-D EBSD images are combined to create a 3D tomographic image. For example, Figure 4 shows tomographic images of grain orientation and grain boundaries in CdTe/CdS solar cells as reported by Stechmann et al. [22]. In Figure 4 (a), grains are colored according to their crystallographic orientation relative to the growth direction shown. The blue colored grains represent (111) oriented grains parallel the growth direction. In Figure 4 (b), grain boundaries are highlighted and colorized according to the disoriented angle ranging from 0° to 60° . Figure 4 (c) and (d) distinguish between random high angle and $\Sigma 3$ twin boundaries, respectively. Finally, further analysis of the $\Sigma 3$ twin boundaries shows that most of them are developed on (111) planes as shown in Figure 4 (e). It is interesting to note that the random grain boundaries shown in Figure 4 (c) form a connected network that surround the grains in Figure 4 (a). In contrast, $\Sigma 3$ twin boundaries in Figure 4 (d) appear more as streaks within the grains shown in Figure 4 (a).

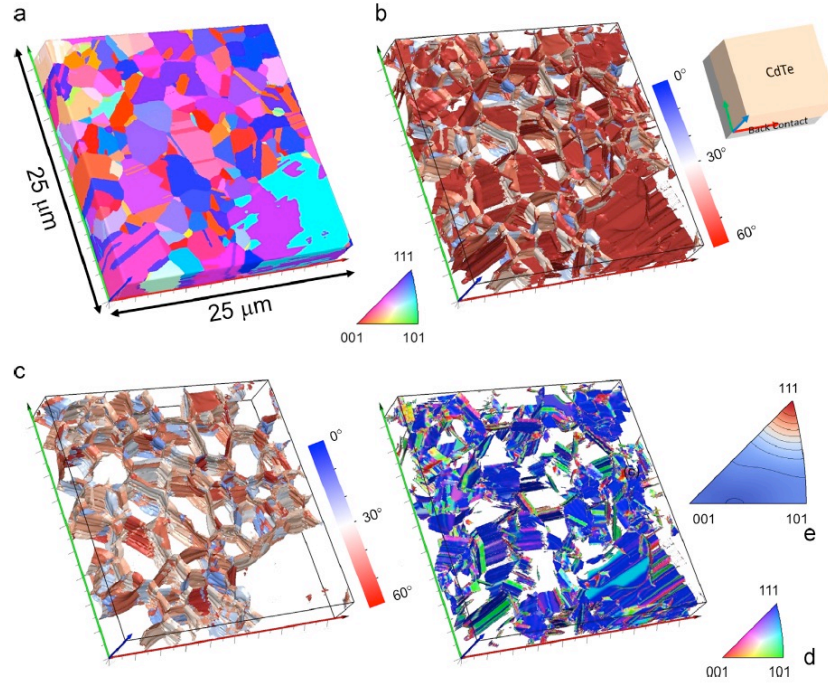


Figure 4: 3D EBSD reconstruction of CdTe layer. (a) Colored grains for the crystallographic orientation, (b) grain boundaries colored according to the disorientation angle, (c) only random high angle grain boundary network, (d) $\Sigma 3$ twin boundary, (e) inverse pole figure[22].

The qualitative difference between $\Sigma 3$ twin and random grain boundaries can also be observed in Figure 5 [9]. The $\Sigma 3$ grain boundaries are shown in light gray whereas the random boundaries are dark bold lines. The $\Sigma 3$ appear as parallel streaks within grains. The random grain boundaries form a connected network which surround grains. Other CSL boundaries such as $\Sigma 5$, $\Sigma 7$ and $\Sigma 9$ are also observed but in much lower density. The most frequently occurring grain boundary is the CSL $\Sigma 3(111)$ twin boundary [23]. Besides the $\Sigma 3$ growth twins, a low density of $\Sigma 9$ (i.e., $\Sigma 3^2$), $\Sigma 27$ (i.e., $\Sigma 3^3$), and $\Sigma 81$ (i.e., $\Sigma 3^4$) twins is also revealed in other reports [24].

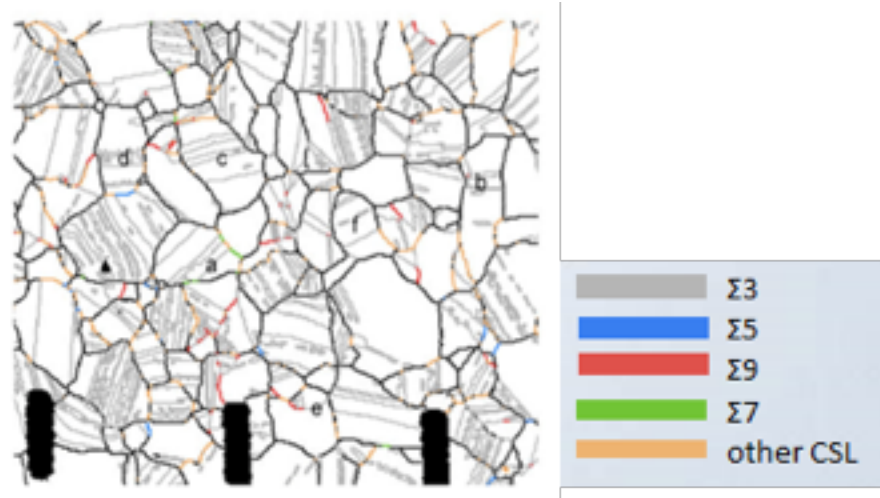


Figure 5: Grain boundary map of a CdTe film via electron back-scatter diffraction (EBSD) [9].

While there are a vast number of GB types and each type may have a different effect, studies have shown that $\Sigma 3$ type of twin GBs in CdTe are usually not active in carrier recombination [25]. On the other hand, non- $\Sigma 3$ types of GBs in CdTe often act as non-radiative recombination centers [23]. However, grain structures in polycrystalline CdTe/CdS systems are complex, involving variations in the grain sizes and shapes, GB types (e.g., Σ value, GB plane, etc.), GB polar characteristics (e.g., Cd-termination or Te-termination), and defects (e.g., vacancies and distortions) along the GB.

To optimize CdTe/CdS solar cell performance, predictive simulations of grain structure evolution is highly desired. In order to create an effective computational method to study the microstructure of CdTe films, it is important to create simulated structures that closely mimic the texture and formation of real films. It is important to characterize the simulated structures and compare to experimental results for validation. Methods that yield validated structures can then be used to study the evolution of structure and finally predict structures based on processing conditions.

2.2 MOLECULAR DYNAMICS

Molecular dynamics is a simulation technique for studying the interactions of atoms in a system. The great computational advantage of classical MD is its high computing efficiency. It provides detailed molecular/atomic level information. The potential energy of the system is calculated using mathematical functions called interatomic potentials. Interatomic potentials are usually written as the series expansion of functional terms that depend on the position of one, two, three, or N atoms at a time. There are different types of interatomic potentials such as the Bond Order potential [26], Lennard-Jones potential [27], Stillinger-Weber (SW) potential [28], and others. In this work, a SW potential is used for all simulations.

2.2.1 Interatomic Potential

A Stillinger-Weber (SW) potential is chosen as the interatomic potential for this research work because it captures accurately the experimental atomic volumes, cohesive energies, and elastic properties of CdTe [29], and predicts the crystalline growth of II-VI compounds correctly [15]. This potential formalism was developed by Frank H. Stillinger and Thomas A. Weber in 1985. Since then, it was widely used for the simulation of silicon and other elements. The SW potential is based on two terms that represent the interaction between two particles and three particles respectively [30] as shown in the equation (2), where θ_{ijk} is the angle formed by the ij bond and the ik bond, and $g(r)$ is the decaying function with a cutoff between the first and the second neighbor shell.

$$V = \frac{1}{2} \sum_{ij} \phi(r_{ij}) + \sum_{ijk} g(r_{ij})g(r_{ik})(\cos\theta_{ijk} + \frac{1}{3})^2 \quad (2)$$

In a system of atoms, this interatomic potential is used in order to obtain the force acting upon each individual atom. Similarly, their acceleration is determined by the net interatomic force

divided by the atom's mass. The velocities can also be calculated by integrating acceleration over time. Once the forces acting on the atoms are known, the positions of the atoms can be updated. Finally, the calculations are performed again for the new positions [31]. Since the potential has been widely used to study grain structures in CdTe/CdS systems [15], [32], [33], knowledge of GB mobilities using the same potential has an additional advantage for comparing to previous studies.

2.2.2 Newton's Law of Particle Motions

The computational task in a MD simulation is to integrate the set of coupled differential equations (Newton's equations) given by,

$$m_i \frac{d\vec{v}_i}{dt} = \vec{F}_i \quad (3)$$

$$\frac{d\vec{r}_i}{dt} = \vec{v}_i \quad (4)$$

where m_i is the mass of atom i , \vec{r}_i and \vec{v}_i are its position and velocity vectors, \vec{F}_i is the force on a given atom i . If there are a total of N_{at} atoms in the system, the force acting on the i^{th} atom at a given time can be obtained from the gradient of the interatomic potential $V(\vec{r}_1, \vec{r}_2, \vec{r}_3, \dots, \vec{r}_{N_{at}})$ as follows,

$$\vec{F}_i = -\vec{\nabla}_i V(\vec{r}_1, \vec{r}_2, \vec{r}_3, \dots, \vec{r}_{N_{at}}) \quad (5)$$

The equation of motion can be solved numerically once the initial conditions and the interaction potentials are defined. The result of the solution are the positions and velocities of all the atoms as a function of time, $\vec{r}_i(t)$, $\vec{v}_i(t)$.

2.2.3 LAMMPS

The Large-scale Atomic/Molecular Massively Parallel Simulator (LAMMPS) [34] is a US Department of Energy (DOE) funded open-source classical molecular dynamics simulation code developed at Sandia National Laboratories that can model 2D or 3D molecular systems with only a few particles or up to millions or billions. This tool can be used to model atomic, polymeric, biological, solid-state (metals, ceramics, oxides), granular, coarse-grained, or macroscopic systems for a variety of different interatomic potentials (force fields) and boundary conditions. It is very efficiently parallelized and can run on any parallel machine that supports the MPI message-passing library including shared-memory boxes, distributed-memory clusters and supercomputers. MD simulations used in this work were performed using LAMMPS.

Chapter 3: Methodologies

3.1 COMPUTER RESOURCES

Two computer clusters called Stampede and Comet were used for the grain boundary migration simulations. The Stampede HPC runs with 522,080 cores, 2.4 GHz Speed and 2,200 Tflop/s and Comet with 24 cores, 2.5 GHz speed and 960 GFLOP/s. These two servers were awarded as part of the NanoMIL team's research allocation provided by the Extreme Science and Engineering Discovery Environment resources. Other resources previously used that also had an impact on this work include Gordon HPC with 16,384 cores, 2.6 GHz Speed and 341 Tflop/s, Red Sky with 22,768 cores, 293 GHz Speed and 264 Tflop/s. Chama with 19,712 cores, 2.6 GHz Speed and 392 Tflop/s and Sky Bridge with 29,568 cores, 2.6 GHz speed, and 600 Tflop/s. Virgo is a high-performance computer (HPC) cluster situated at the Department of Electrical Engineering at the University of Texas at El Paso. This cluster runs on a Beowulf Cluster with 160 cores, 2.65 GHz speed and 139 Peak GFLOP/s. Finally, our group has access to Lonestar 5 with 24 cores per computing node, 2.6 GHz speed as part of TACC resource allocation that is available to UT System researchers for our ongoing research.

Post analysis of simulated data includes the analysis of grain boundary migration and the execution of an algorithm that computes information regarding grain orientation [19]. These computations were performed using MATLAB software which is a numerical computing environment and programming language.

3.2 CONDITIONS FOR POLY-CRYSTALLINE GROWTH

Polycrystalline growth, developed by Aguirre et al. [32], in this study was achieved by depositing Cd and S atoms on an amorphous CdS substrate in analogy to molecular-beam epitaxy.

Although the substrate was amorphous, the deposited Cd and S atoms formed “naturally” into a polycrystalline film without any assumptions regarding the structure of the atoms. Cd and Te atoms were subsequently then deposited on the CdS layer to create a polycrystalline CdTe/CdS heterostructure as shown in Figure 6.

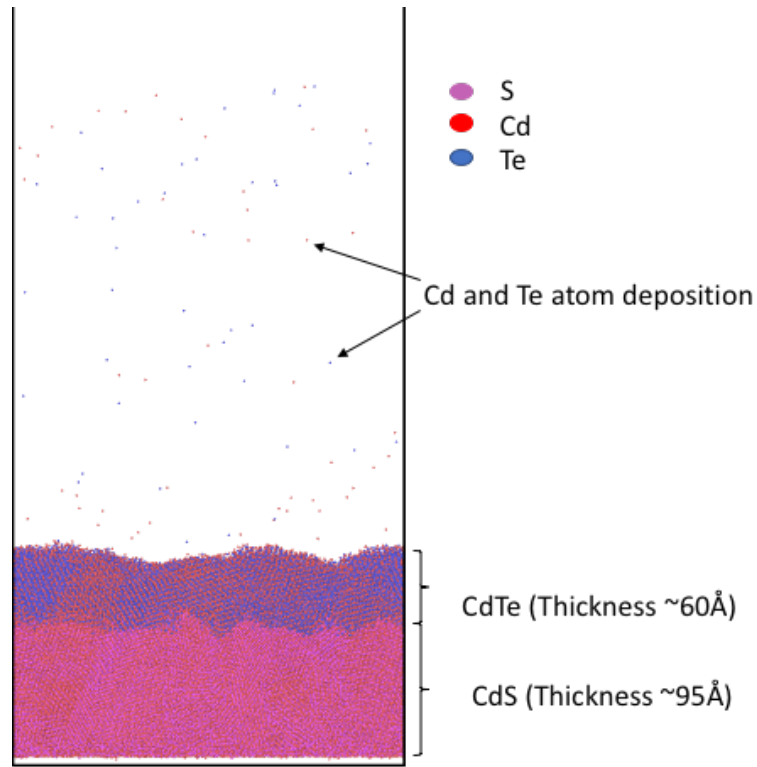


Figure 6: CdTe/CdS heterostructure grown by CdTe deposition on CdS layer.

This amorphous layer was constructed by heating a thin layer of single crystal CdS material up to the melting point. As seen in Figure 7(a), this thin layer was held between two fixed layers. The fixed layers were kept immobile, i.e., no temperature was applied to them so that these layers can prevent the atoms in the middle layer from vaporization at high temperature. To make the middle layer amorphous, ~ 2200 K temperature was applied there. The resulting amorphous structure is represented in Figure 7(b) where the yellow shaded area was then used as a substrate for polycrystalline deposition.

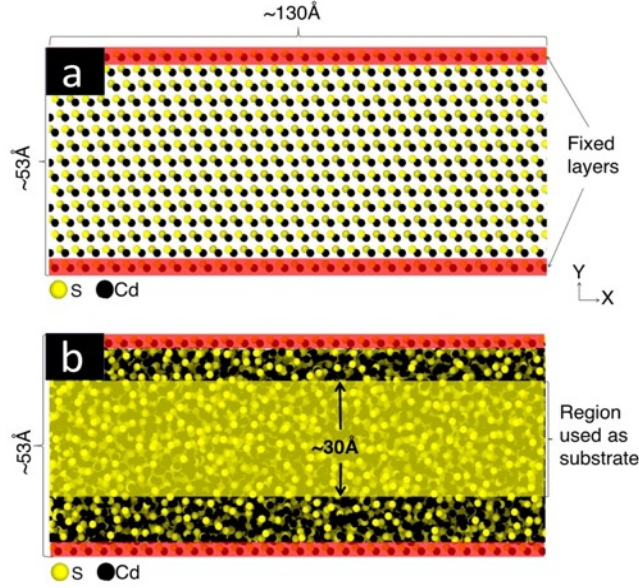


Figure 7. (a) Single crystal CdS layer and (b) amorphous CdS after melting phase.

After the amorphous layer was created, CdS and CdTe were successively deposited in order to achieve the growth of the crystal layers. Initial growth of CdS on top of the amorphous layer is shown in Figure 8(a). Notice that CdS successfully nucleated into grains with zincblende and wurtzite regions as indicated in Figure 8(b) by the blue and red regions, respectively. After the CdS deposition the polycrystalline layer was prepared for CdTe deposition. Figure 7 and Figure 8 show only a portion of the full substrate for better visualization. The real dimensions of the CdS amorphous substrate are $300\text{\AA} \times 100\text{\AA} \times 53\text{\AA}$ for X, Y and Z, respectively. The deposition temperature and deposition rate were 1200 K and 4 \AA/ns , respectively. Canonical ensemble thermostat was used for the simulation. Single adatoms were injected perpendicularly toward the substrate surface. These experimental conditions were previously set up by Aguirre et al. [32].

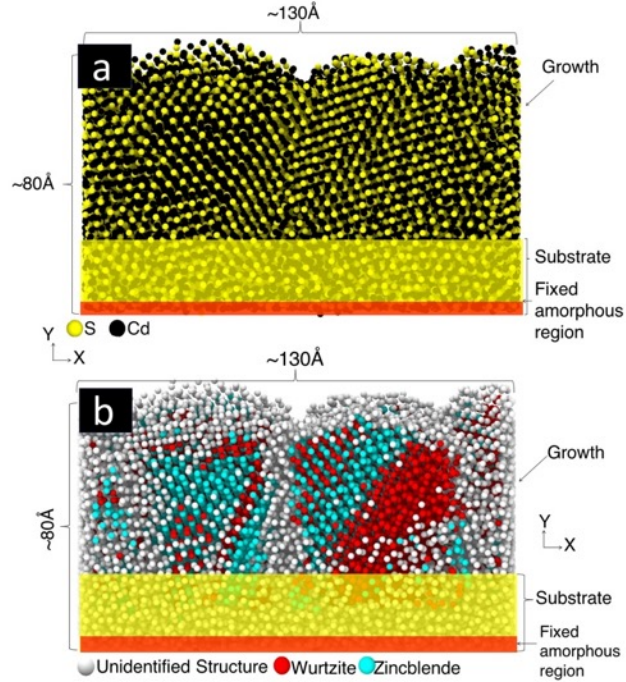


Figure 8. (a) Atomic and (b) structure maps of the initial stages of growth of CdS on the amorphous layer.

3.3 CREATION OF CdTe BI-CRYSTALS

Different types of grain boundary structures can be constructed with a tool in LAMMPS called “CreateAtoms”. For example, Figure 9 shows $\Sigma 3(111)$, $\Sigma 7(111)$, and $\Sigma 11(311)$ grain boundaries created using CreateAtoms by Dr. Xiaowang Zhou from Sandia National Laboratories. The black and purple circles represent cadmium and tellurium atoms, respectively. The $\Sigma 3$ and $\Sigma 7$ grain boundaries are in the (111) plane along with the y-direction which is represented by [111] and the $\Sigma 11$ grain boundary is placed in the (311) plane along with the y-direction i.e. with [111] direction. In Figure 9(a) and Figure 9(c), the orange broken line highlights the location of the boundary between grains. For simplicity, the grain boundaries will be referenced only as $\Sigma 3$, $\Sigma 7$, and $\Sigma 11$ respectively throughout this thesis.

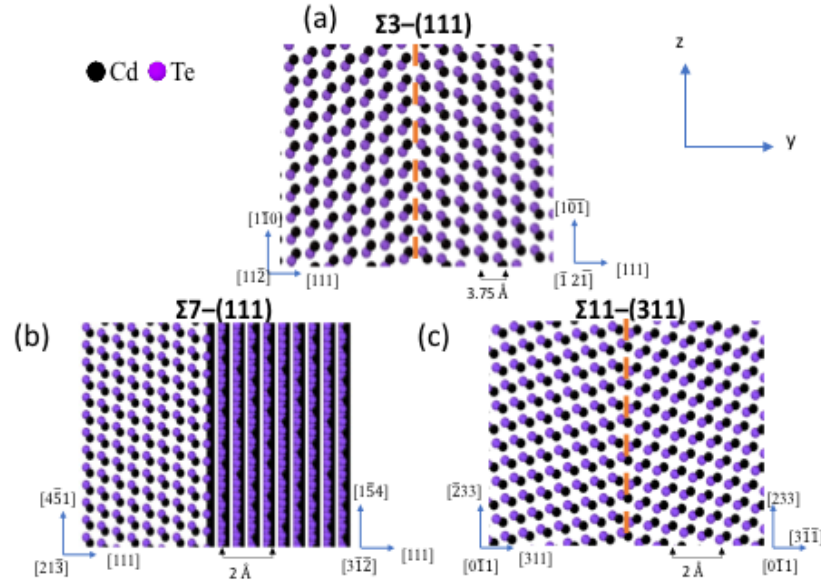


Figure 9. Grain boundary structure of (a) $\Sigma 3(111)$, (b) $\Sigma 3(111)$ and (c) $\Sigma 3(111)$.

3.4 ALGORITHM FOR BOUNDARY MIGRATION

Janssens, et al., developed a method to compute the mobility of flat grain boundaries using an artificial driving force on the boundary [35]. The main idea of the method is to start with a bi-crystal with a predefined grain boundary. Potential energy is added to the atoms in one grain while keeping the atoms in the other grain at zero potential. This will cause the atoms near the boundary to have an energy difference which creates a driving force to reduce the potential energy of atoms near the boundary by pushing the boundary towards the interior of the grain having high potential energy. Thus, grain boundary migration occurs. While Janssens' approach worked with only FCC structures, the method was recently generalized by Dr. Zhou to work with other crystals [36].

3.5 CONFIGURATION FOR BOUNDARY MIGRATION IN CdTe BI-CRYSTALS

Janssens approach was implemented in LAMMPS to study the migration of 3 grain boundaries in CdTe. For example, in Figure 10, a potential energy is added to grain 1 while grain 2 has no potential energy. Therefore, a potential difference formed at the grain boundary which creates a driving force to move the grain boundary. As a result, grain 1 shrinks to reduce the

potential energy and grain 2 expands. The detailed explanation of the potential energy and the order parameter with the necessary formulae is provided by Aguirre et al. [36].

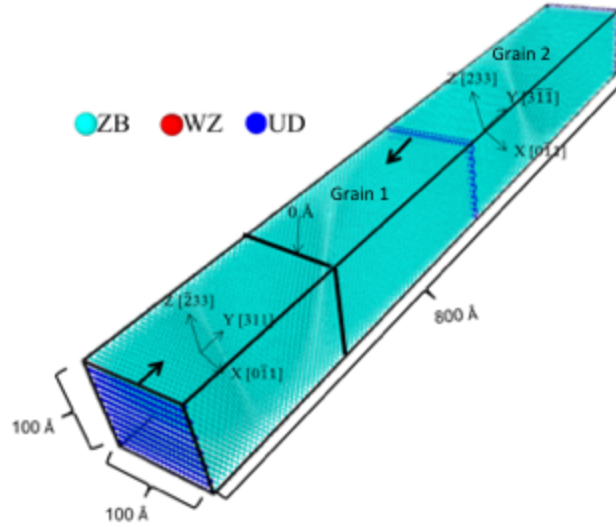


Figure 10. Grain boundary migration configuration of $\Sigma 11$

MD Simulations were performed on three CdTe grain boundaries $\Sigma 3(111)$, $\Sigma 7(111)$ and $\Sigma 11(311)$ as already published by Aguirre et al.[36]. The simulations consisted of a simulation box of ~ 100 Å in x, ~ 800 Å in y, and 100 Å in z. The simulation box contained two CdTe grains with two grain boundaries parallel to the X-Z plane under the periodic boundary conditions. One grain boundary was located at the center of the simulation box which is in between grain 1 and grain 2 as shown in Figure 10. The second grain boundary was located at the periodic boundary. The resulting structure for $\Sigma 11$ is shown in Figure 10. Notice that light blue, red and dark blue atoms represent atoms within zincblende (ZB), wurtzite (WZ) and undetermined (UD) lattice sites, respectively. Here, UD means that the atoms were not determined to belong to the ZB or the WZ structure.

3.6 GRAIN STRUCTURE AND GRAIN BOUNDARY ANALYSIS

Three-dimensional time evolved visualization of simulated data including atomic species maps and structure maps were generated using the Open Visualization Tool (Ovito) [17]. Ovito is a scientific visualization and analysis software for atomistic simulation data developed by Alexander Stukowski at Darmstadt University of Technology, Germany. Ovito can provide information regarding the crystal structure, dislocations, common neighbor analysis, centrosymmetry parameter, etc. The program is open-source and freely available for all major platforms. The centrosymmetry parameter is used to determine whether an atom is inside a perfect lattice or at a local defect. Moreover, the common neighbor analysis calculates the local crystal structure surrounding an atom [37].

3.7 GRAIN ORIENTATION ANALYSIS

A computation tool called the “Grain Tracking Algorithm” (GTA) developed by Panzarino et. al. [19] is a post-processing algorithm which computes information regarding the orientation of grains in a material. The algorithm uses the atom positions, centrosymmetry parameter and the common neighbor analysis values [37] to identify the crystalline structures. GTA outputs the grain orientation, grain pole figures, displacement vector components which provide the crystallographic orientation information etc.

The measured orientations of each grain are visualized with colored orientation maps. For example, the orientation of various grains within a polycrystalline CdTe/CdS structure was analyzed using the Grain Tracking Algorithm as shown in Figure 11. in Figure 11 (a) shows several different grains of Te atoms as indicated by the different colors to represent the crystallographic orientations of each grain according to the color map in in Figure 11 (b). In this particular example, the simulation direction was $\{010\}$, which points vertically down (or up), parallel to the y-

direction. From the color map shown in in Figure 11(b), it is observed that the red colored grains have a $\{001\}$ orientation, whereas the blue colored grains have a $\{111\}$ orientation, with respect to the y-direction indicated in the in Figure 11(a).

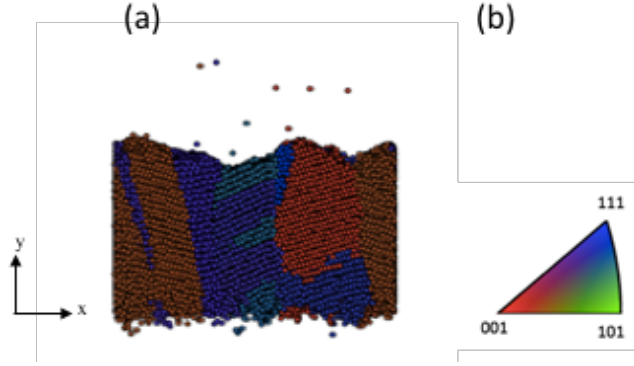


Figure 11. (a) Visualization of polycrystalline Te atomistic structure with the [010] simulation direction, (b) inverse pole figure representing crystal orientation.

The GTA tool provides the pole figure and the inverse pole figure to explain the visual representations of the crystal orientations. The pole figure depicts the positions and intensities of the crystallographic orientations through a stereographic projection. A stereographic projection is needed to understand different plane directions in the crystal and also the angular relationships between different planes and axes. Additionally, the inverse pole figure also represents the textural information by depicting the selected directions in relation to the crystal axes. This is also called the axes distribution chart. In GTA, the colored inverse pole figure is used.

Furthermore, the GTA tool provides the components of displacement vectors for atoms in different grains. For FCC, the displacement vectors are calculated as follows. There are four neighbor atoms in FCC lattice whose directional vectors are positioned approximately 60° apart from the original vector as shown in Figure 12. From these four vectors, two directions which are perpendicular to their counterparts and contain two nearest neighbors in the same plane can be calculated. Then, from their cross product, the third direction can be calculated.

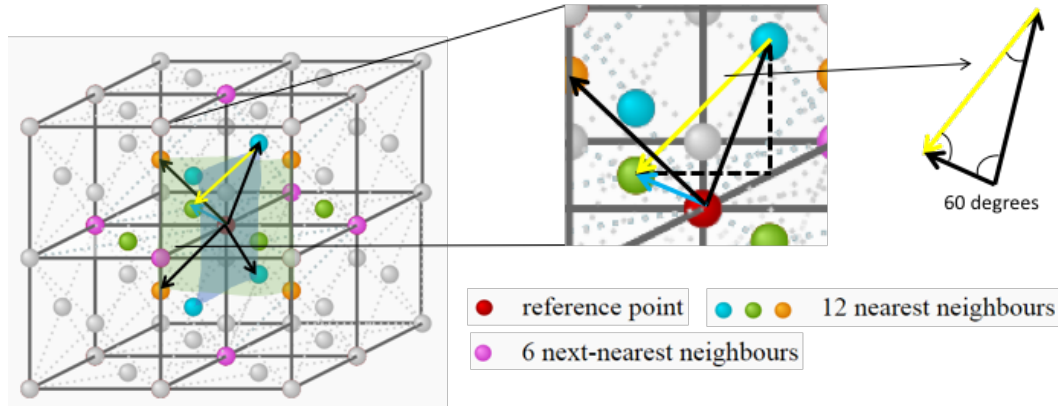


Figure 12. Displacement vector calculation for FCC. [38]

The GTA tool has several limitations. Firstly, GTA only works for FCC and BCC but no other structures such as zinc blende or wurtzite. This requires that zinc blende data be conditioned by removing one of the FCC sub-lattices before inputting into GTA. Moreover, wurtzite phases need to be removed. Another limitation is that GTA does not execute when the number of amorphous atoms exceed $\sim 10^3$. Therefore, highly disorders atoms need to be removed prior to inputting into GTA. A visualization limitation is that the output showing the texture of the sample appears cubic even the input structure is a cuboid structure. To observe the orientations clearly, the samples were sliced into cubic parts and the output was visualized as a composite of the sliced cubic structures. Finally, difficulties were faced in feeding large centrosymmetry values into GTA and caused algorithm to stop execution and not give output. The values were therefore scaled by a factor of 10^{-5} .

To get the proper crystal orientation from the GTA tool, energy was minimized by iteratively adjusting atom coordinates using LAMMPS. Energy minimization was done to ensure the minimum local potential energy in the crystal structure. In this process, simulated annealing was performed at a high temperature (1200 K) for a while (4ns) and then the temperature was

lowered to 50 K. Energy minimization is important to get the position of atoms closer to their equilibrium position within a crystal.

Chapter 4: Results

4.1 ANALYSIS OF CdTe/CdS POLYCRYSTALLINE GROWTH

This section analyzes the growth evolution of the polycrystalline CdTe/CdS heterostructure introduced in the previous chapter. This analysis is key to understanding the formation of granular microstructures by qualitatively studying the motion of grain boundaries and other crystal growth phenomena. Key stages of growth are observed such crystal nucleation, coalescence, and coarsening. Importantly, the early stages of heteroepitaxial growth of CdTe on CdS is also analyzed. 50 separate images were of the CdS and CdTe growth from the top view were generated with a time difference of 2 ns between each image. A movie was generated from this time sequence to qualitatively observe the motion of the atoms and formation of grains and grain boundaries.

At the first stages of CdS growth (2.1 nm), small zinc blende (ZB) and wurtzite (WZ) grains nucleate with random orientations and sizes ranging from 5 to 460 atoms as shown in Figure 13(a). The nucleation density is approximately $1.5 \times 10^{13} \text{ cm}^{-2}$. This results in a sparsely nucleated surface with most of the surface area covered by amorphous (disordered) atoms. The number of ZB (blue) and WZ (red) grains are approximately equal. The crystalline atoms are essentially immobile compared to the disordered atoms (white) which exhibit much higher mobility.

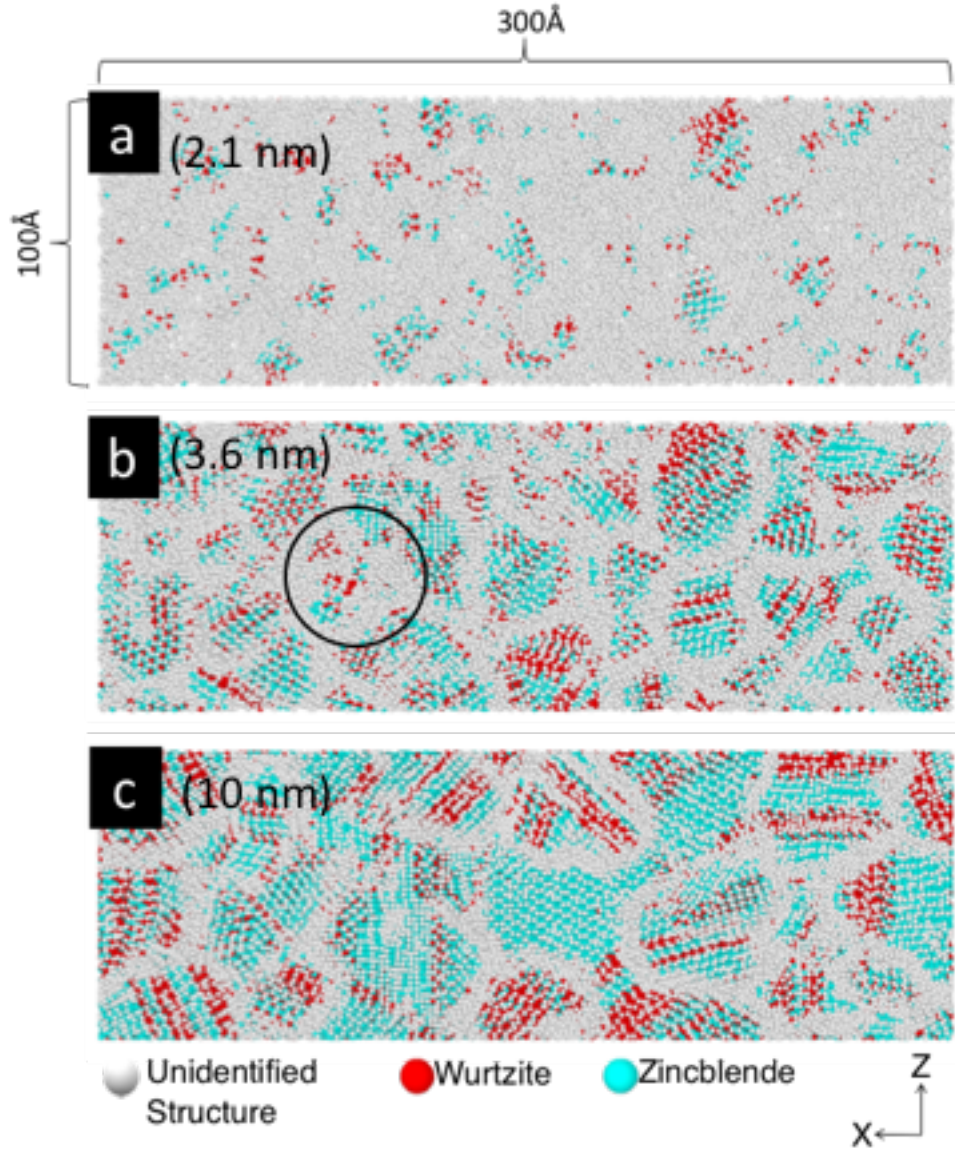


Figure 13. Top view of the CdS structure at thicknesses (times) of (a) 2.1 nm (2 ns), (b) 3.6 nm (12 ns), and (c) 10 nm (48 ns).

The radius of all of the nuclei increase with time indicating that the critical radius is very small: No nuclei were observed to lose atoms over time. The larger nuclei grow by adding atoms to their surface areas. This allows the larger grains to grow at a faster rate compared to the smaller nuclei. In contrast, the smaller nuclei grow by coalescing with neighboring nuclei. In one case, at a thickness of 3.6 nm (12 ns time), four nuclei coalesced into one grain as indicated by the circle

in Figure 13(b). It is also observed that the ZB phases grow much faster compared to the WZ. After the initial growth by coalescence in the sparse film, growth continues by addition of atoms to the surface of the grains until the substrate is mainly covered by crystalline grains and a network of grain boundaries between them. After this point, growth occurs by coalescence of large grains or motion of grain boundaries with the thickness of 10nm shown in Figure 13(c). Two general types of grain boundaries are observed: random and correlated. The random grain boundaries are composed of highly disordered atoms, shown with white colored atoms in Figure 13(c) and separate two grains. These grain boundaries show the grain boundary network which shows similarities with the experimental results of random high angle grain boundary network [22] discussed in the previous section. The correlated grain boundaries are atomically thin boundaries between two grains and are highly coherent, e.g., twin boundaries. These can be observed in Figure 13(c) as red WZ streaks or lines which could be similar to the experimental results of $\Sigma 3$ twin boundaries. Figure 13(c) represents the last image before deposition of CdTe.

Deposition of CdTe on the CdS layer occurs at approximately 10.2 nm (48.4 ns). In other words, the atom flux is switched from Cd-S to Cd-Te at 48.4 ns (Figure 14(a)). However, nucleation and growth of CdTe does not occur immediately upon arrival of Cd and Te adatoms to the CdS surface. Instead, incident Cd and Te atoms start to accumulate on the random grain boundaries in amorphous form. This is observed in Figure 14(b) which shows an accumulation of disordered surface atoms with minimal change in the crystalline grains. (Figure 14(b) is 8 ns after the flux is switched to CdTe.)

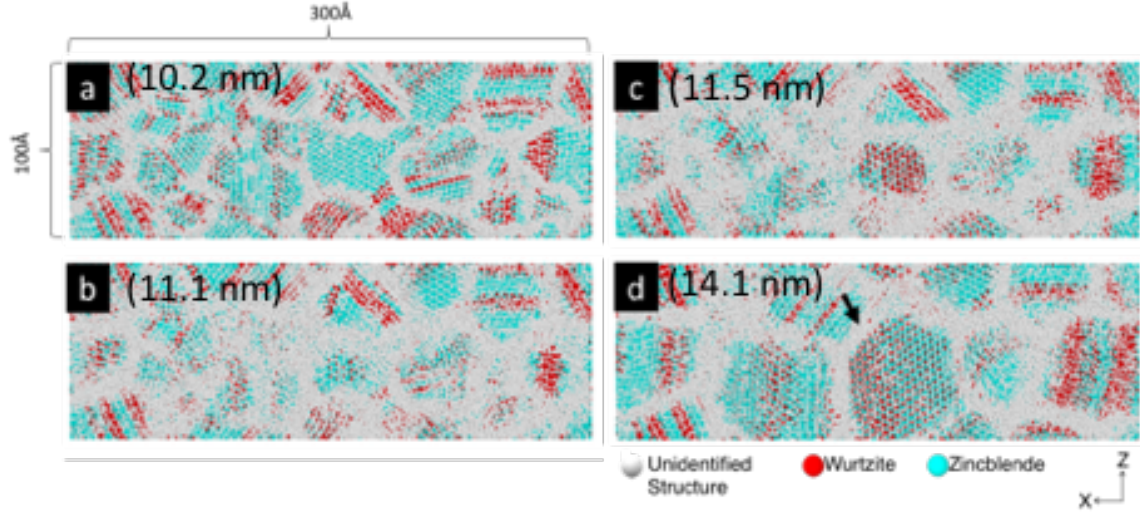


Figure 14: Top view of the CdTe growth at sample thickness (times) of (a) 10.2 nm (48.4 ns) (b) 11.1 nm (56.4 ns), (c) 11.5 nm (58.4 ns), and (d) 14.1 nm (68.4 ns).

Importantly, Figure 14(c) (11.5 nm and 2 ns after Figure 14(b)) captures the onset of rapid CdTe grain growth which is much faster compared to previous growth. Finally, Figure 14(d) (14.1 nm) shows how the CdTe grains rapidly evolved within 10 ns. Numerous grain boundary triple-junctions can be observed throughout the film. The CdTe grains are more faceted compared to the CdS grains as indicated by the arrow in Figure 14(d).

Figure 15 is a sliced view of the final CdS/CdTe heterostructure with a total thickness of 14.2 nm. These slices show the difference in grain size. The bottom slice shows that the grains in the CdS layer are relatively smaller and more numerous compared to the CdTe layer (top slice). Grain sizes increase with growth and thickness of the material. The middle slice contains the CdTe/CdS interface. The random grain boundaries with highly disorder atoms (white colored atoms) are also observed here which form boundary networks as mentioned in the experimental results. Red WZ streaks are also noticeable at the top of the middle layer.

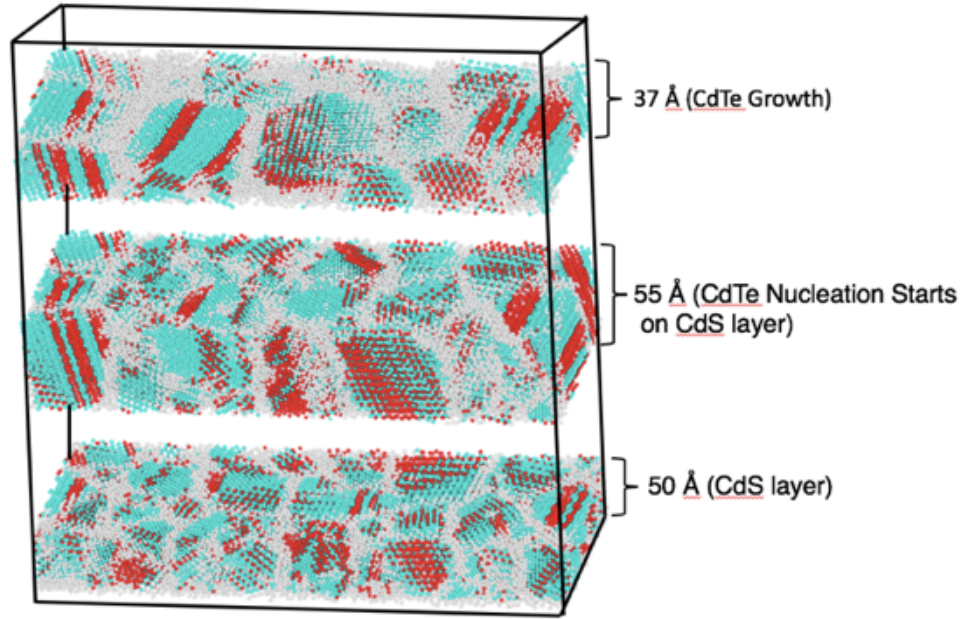


Figure 15. Slices of CdTe/CdS heterostructure at 68.4 ns.

4.2 ANALYSIS OF CRYSTAL ORIENTATION

4.2.1 Validation of GTA Grain Orientation Tool

In this section, the orientation of the grains in a $\Sigma 7(111)$ bi-crystal is analyzed to validate the output from GTA. The results were obtained from the $\Sigma 7(111)$ bi-crystal having the simulation box size of ~ 100 Å in X- axis, ~ 220 Å in Y-axis and ~ 100 Å in Z-axis. Figure 16 (a) is the output from Ovito where the FCC structure of Cd atoms are colored green and the white colored central grain boundary separates the two grains. Both grains have $[111]$ direction along the Y-direction. Figure 16 (b) shows outputs from GTA with the simulation direction parallel to the Y-direction (blue colored) and X-Y-direction respectively. The inverse pole figure shown in Figure 16 (c) provides the plane information according to the simulation direction. The GTA output, showing the same blue color for both the grains, describes that both the grains have $[111]$ directions along the Y-direction. This result is correct as it matches the orientation of the predefined $\Sigma 7(111)$ bi-crystal. When the simulation direction is $[110]$, the output shows different colored grain orientations.

Additionally, the positive pole figure is shown in Figure 16(d) for $\Sigma 7(111)$ from the $[001]$ direction to describe the positions and intensities of the specific crystallographic orientations. The red dots, called poles, indicate the position of the crystallographic orientation which are the plane of $\langle 111 \rangle$ family for $\Sigma 7(111)$ depicting the (001) stereographic projection.

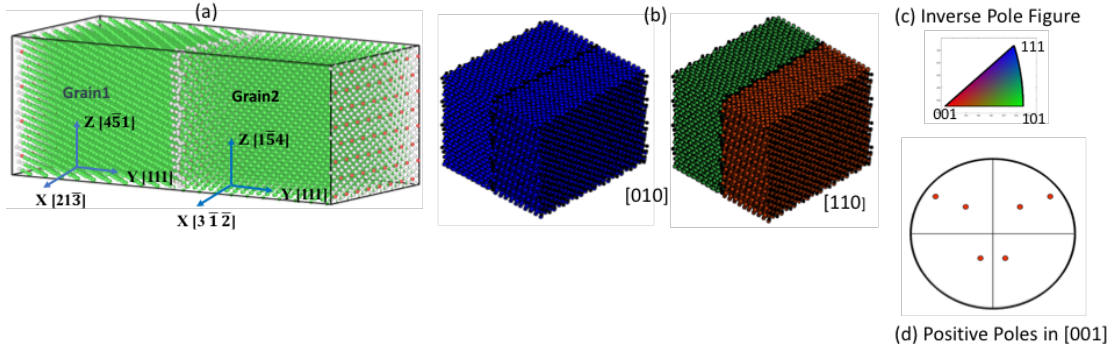


Figure 16. Crystal orientation of $\Sigma 7(111)$ visualized by (a) Ovito, (b) GTA grain orientation, (c) Inverse pole figure, d) positive pole figure in $[001]$ direction.

4.2.2 Texture Analysis of Polycrystalline CdTe/CdS Sample

This section calculates the orientation of the CdTe grains from the polycrystalline CdTe/CdS sample using the GTA tool. This analysis is important to identify the type of boundaries in the material. Figure 17 contains corresponding grain structure and grain orientation maps of the Cd-sublattice of the CdTe layer. The structure maps were created using Ovito whereas the orientation maps were created using the GTA tool. FCC, WZ and ZB structures can be observed in the structure maps contained in Figure 17(a). The orientations of the grains are observed in Figure 17(b). In order to obtain output from the GTA tool, the CdTe data was first conditioned by performing an energy minimization of the sample, removing the Te atoms to create the Cd-sublattice, and removing disordered atoms. For the energy minimization, the annealing temperature was $\sim 1200\text{K}$, the annealing time was 4 ns and the final temperature was 50K. In Figure 17(b), different grain orientations are displayed by using different colors. For example, the red colored portion describes the (001) plane when the simulation direction is $[010]$ which is y-

direction here which is normal to both the x and z direction. This finding can be used to quantify the types of grain boundaries.

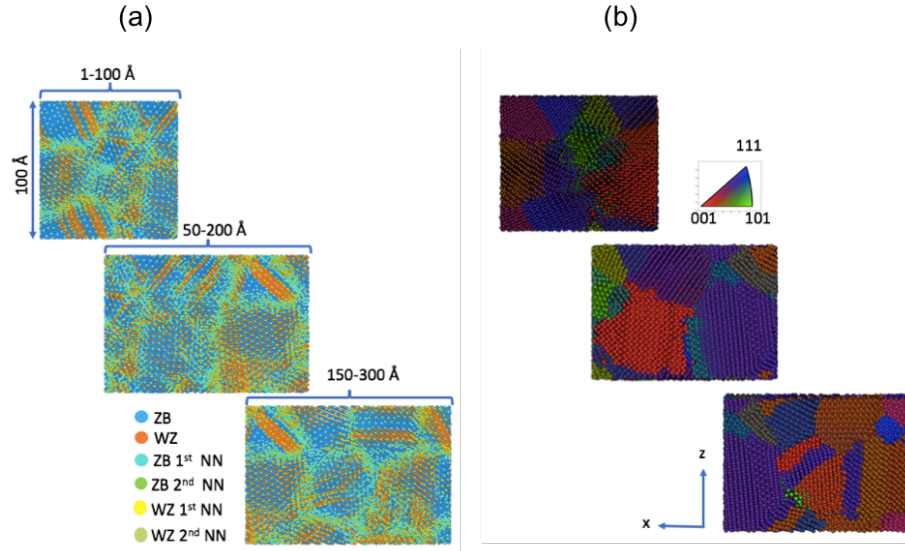


Figure 17. (a) Crystal structure visualized by OVITO, (b) Crystal orientation by GTA.

A close comparison between the Ovito and GTA outputs as shown in Figure 18 validates the visual orientation output of the GTA tool. The blue circled area Figure 18(b) in represents a grain having (001) orientation. The corresponding blue circled region in Ovito as shown in Figure 18(a) seems almost cubic which is a known (001) plane orientation. This represents the same orientation in both Ovito and GTA and confirms that GTA is providing the correct grain orientation output.

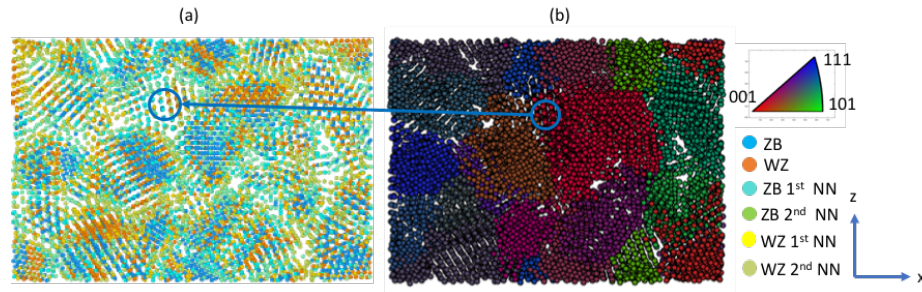


Figure 18: Validation of GTA output through comparison of visualization method (a) Ovito output, (b) GTA output.

4.3 ANALYSIS OF GRAIN BOUNDARY MIGRATION IN CdTe BI-CRYSTALS

Knowing grain boundary mobilities, along with grain boundary energies, enables the prediction of the evolution of polycrystalline microstructures such as grain sizes and grain boundary types under processing and operating conditions. Knowledge of grain boundary mobilities is essential to extend the time and length scales of high-level simulations such as molecular dynamics (MD) simulations to engineering scales, which can impact many technologically important applications. In this section, the effect of crystal structure and temperature on grain boundary migration is discussed.

To obtain the results showing grain boundary migration, the potential energy of 1 eV was implemented into one grain and the grain boundary migration occurred according to the approach mentioned in the previous section. The results presented in this thesis were achieved from the MD simulations executed at 1000 K, 1200 K and 1800K temperature.

The migration of a grain boundary depends on its detailed structure. Figure 19 depicts the boundary migration at the temperature 1800 K and energy 1eV. The boundary migration behavior of $\Sigma 3(111)$ is shown in the Figure 19 (a). It is observed that the movement of $\Sigma 3(111)$ grain boundary is negligible within the first 0.9ns. At the same temperature and energy, $\Sigma 7(111)$ and $\Sigma 11(311)$ grain boundaries can move faster over the same time period due to their lower activation energy as shown in Figure 19(b) and (c) respectively. Additionally, coherent grain boundary could be another reason for the low mobility of $\Sigma 3(111)$. A $\Sigma 3(111)$ grain boundary consists of two grains separated by an angle of 60° having symmetric crystal orientation which is why $\Sigma 3(111)$ is called a coherent boundary. However, this characteristic is not seen in $\Sigma 7(111)$ and $\Sigma 11(311)$ grain boundaries. Furthermore, comparing Figure 19 (b) and (c), it is observed that $\Sigma 11(311)$ moves faster than $\Sigma 7(111)$.

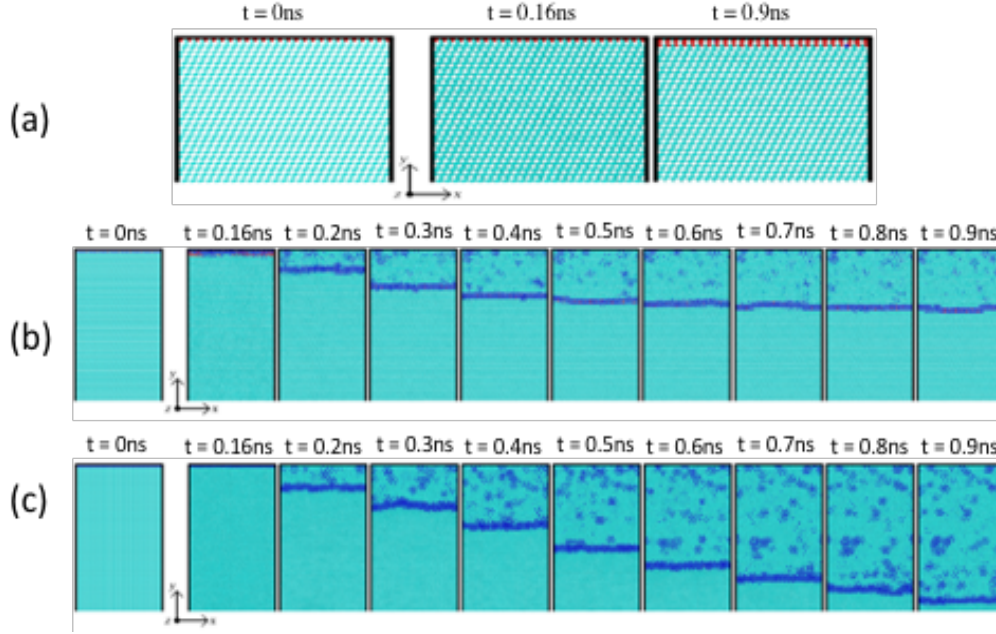


Figure 19. Grain boundary migration of (a) $\Sigma 3(111)$, (b) $\Sigma 7(111)$, (c) $\Sigma 11(311)$ grain boundaries at 1800 K and added energy of 1 eV.

In order to understand the atomic motion in the grain boundary migration it is important to study the fundamental mechanism of the grain boundaries. In this thesis, the fundamental mechanism of $\Sigma 11(311)$ has been analyzed. However, in $\Sigma 11(311)$, the grain boundary migration occurs mainly by the rotational motion between the atomic pairs which look like dumbbell structures shown in Figure 20 where the blue and red spheres represent the Te and Cd atoms respectively. Once one atomic layer was fully reconstructed, the next atomic layer motion began. As the propagation occurs simultaneously along the Y-Z plane, the formation of kinks is not noticeable in $\Sigma 11(311)$ grain boundary.

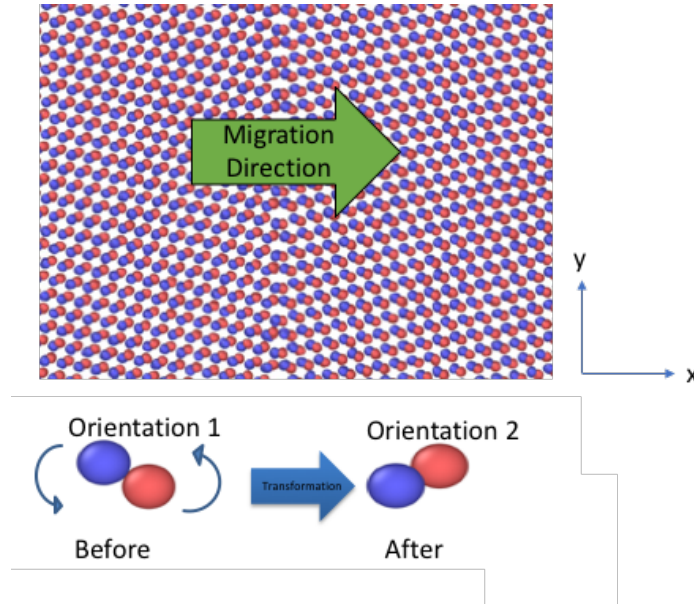
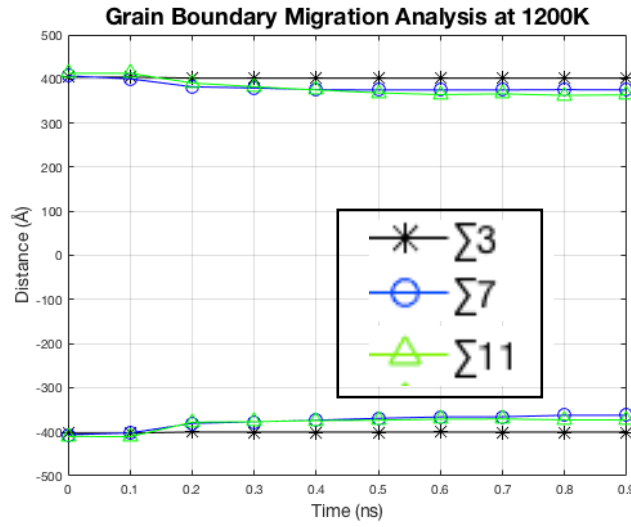


Figure 20. Grain boundary migration mechanism of $\Sigma 11(311)$ at 1000 K and added energy of 1 eV.

Temperature difference has an impact on the grain boundary migration which can be clearly observed from the migration of $\Sigma 7(111)$ and $\Sigma 11(311)$ grain boundaries when different temperatures were applied. Figure 21 reveals the grain boundary migration distance over time which is a graphical representation of Figure 19. The migration distances of the $\Sigma 7(111)$ and $\Sigma 11(311)$ grain boundaries increase when temperature is increased. For $\Sigma 7(111)$, the observed migration distance is $\sim 10 \text{ \AA}$ at 1200 K temperature which increases to $\sim 80 \text{ \AA}$ when the temperature is raised to 1800 K. However, the migration is faster in $\Sigma 11(311)$ where the distance increases from $\sim 10 \text{ \AA}$ to $\sim 180 \text{ \AA}$ for the same temperature shift. These results are consistent with the work of Aguirre et al. [36] which showed that within the temperature range of 300 K- 2200K and energies up to 2 eV, the migration distances of the $\Sigma 7$ and $\Sigma 11$ grain boundaries increase when temperature and driving energy are increased. However, for $\Sigma 3(111)$, the migration remains small for the temperature ranges and time scales used for this simulation.

(a)



(b)

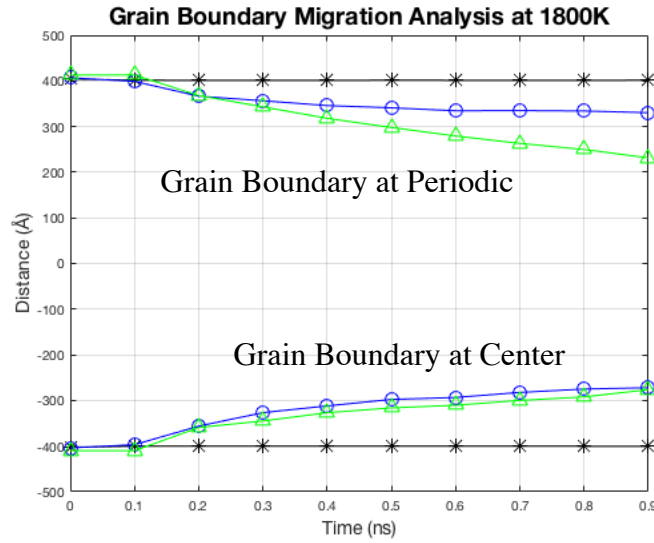


Figure 21. Graphical representation of grain boundary motion of $\Sigma 3(111)$, $\Sigma 7(111)$ and $\Sigma 11(311)$ (a) at 1200 K and (b) at 1800 K.

Chapter 5: Future Work

5.1 RESEARCH GOAL

In this work, the grain and grain boundary formation and fundamental mechanism were studied. The grain evolution of naturally grown polycrystalline CdS and CdTe was analyzed with no prior assumption at an atomic scale using molecular dynamics simulations which mimics the experimental results. Orientation of the grains within the polycrystalline CdTe/CdS was successfully computed using a combination of computational tools. However, the type of grain boundaries in these chalcogenide polycrystalline materials has not yet been identified. Furthermore, the grain boundary migration of the constructed $\Sigma 3(111)$, $\Sigma 7(111)$ and $\Sigma 11(311)$ grain boundaries was analyzed in terms of the effects of crystal structure and temperature on the motion.

Future work will consist of quantifying the grain boundary types of the simulated polycrystalline structures, characterizing the grain boundary statistics and dynamics, and disseminating the findings. It is important to know the grain boundary types grown during the simulated polycrystalline CdTe to understand the nature of the film and design better quality CdTe films. An algorithm to detect the grain boundary types is needed in order to do so. An already established approach [19] for FCC and BCC structures will be modified for CdTe and CdS structures. A tool will be developed which will jointly provide the information of the CdTe and CdS structures regarding their grain orientation, grain size, number of grains and types of grain boundaries. It will be a big step forward for atomic level analysis of grain boundaries, particularly for “naturally grown” layers of photovoltaic thin film where no prior assumptions were used, for which such analysis is still unavailable. The block diagram shown in Figure 22 represents the proposed methodology.

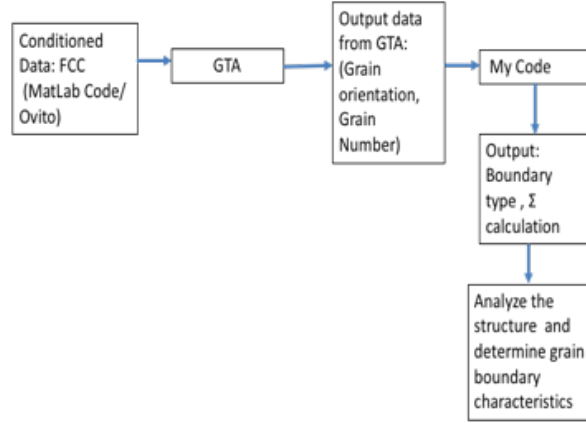


Figure 22. Block diagram of the proposed work

The following steps will be performed to accomplish the proposed methodology. First, the energy needs to be minimized to get the position of atoms closer to their equilibrium position within a crystal. For energy minimization, the proper conditions such as annealing temperature and time will be set for the MD simulation which will be executed using the LAMMPS code. Secondly, to feed the sample to the GTA tool, the crystalline and non-crystalline atoms will be identified in the sample input file consisting of the atomic positions. To accomplish this step, the required crystal structure identification information will be obtained from Ovito by using common neighbor analysis and centrosymmetry parameters. Then, the disordered atoms will be removed.

ITEM:	TIMESTEP											
	0											
ITEM:	NUMBER	OF	ATOMS									
	26880											
ITEM:	BOX	BOUNDS		pp	pp	pp						
	-0.5	96.4538269										
	-0.5	223.9044952										
	-0.5	83.4644776										
ITEM:	ATOMS											
a1	a2	a3	b1	b2	b3	c1	c2	c3	gnum	x	y	z
0.8017836	0.5773505	0.1543032	0.2672612	-0.5773506	0.7715166	0.5345223	-0.5773506	-0.6172133	1	34.6263619	178.588562	64.972519
0.5345226	-0.5773503	-0.6172134	0.267261	-0.5773502	0.771517	-0.8017839	-0.57735	-0.1543034	1	20.7758198	171.108429	80.965744
-0.5345223	-0.5773502	-0.6172136	0.8017837	-0.5773504	-0.1543031	-0.2672616	-0.5773503	0.7715166	2	79.6406555	66.386322	70.9699784
0.2672612	0.5773504	-0.7715166	0.8017838	-0.5773502	-0.1543036	-0.5345225	-0.5773502	-0.6172135	2	18.1788445	73.866478	80.4659577
0.8017835	0.5773505	0.1543035	0.5345223	-0.5773506	-0.6172133	-0.2672609	0.5773505	-0.7715168	1	71.849701	163.6282807	74.4684983
-0.801784	-0.5773498	-0.1543035	0.5345228	-0.5773502	-0.6172133	0.2672609	-0.57735	0.7715171	1	31.1637306	212.2492371	40.982666
0.5345224	0.5773502	0.6172136	0.8017836	-0.5773504	-0.1543036	0.2672613	0.5773503	-0.7715168	2	26.8354321	107.527153	62.4735756
0.2672616	0.5773501	-0.7715168	0.5345224	0.5773504	0.6172134	0.8017838	-0.5773504	-0.1543029	2	12.9848872	10.2852049	39.4832993

Figure 23. Sample of orientation data from GTA

The third step is calculating the grain orientation to identify the local crystallographic orientation of the grains. This step will be performed with the GTA tool. The GTA generates the orientation information in a tabular format as shown in Figure 23 where (a1, a2, a3), (b1, b2, b3) and (c1, c2, c3) represent the displacement vectors for the three coordinate axes and (x,y,z) represents the atomic position. Atoms having the same orientation displacement vectors belong to the same grain and have the same grain number which is displayed in the 'gnum' column.

In step four, the neighboring grains will be identified to calculate the grain boundary type. For that, the approach is to write a code that will identify grains by using atomic position information. By using the grain orientation and the identity of the neighboring grains, the grain boundary type can be calculated. The difference in the angle of rotation between two adjacent grains will give the type of grain boundary whether it is high angle or low angle.

Additionally, a thorough literature review will be conducted to find out the methodology to calculate the Σ values in a polycrystalline structure. One of the approaches to develop this algorithm will be following the EBSD technique which provides the experimental information regarding grain structure, grain boundary characteristics, crystallographic texture, phase discrimination and distribution etc. In this technique, the electron backscattered pattern (EBSP) is formed first by using Bragg's Law and then the phase and orientation of a crystal is obtained from the EBSP. The EBSD data visualization and analysis method will therefore be studied further in order to develop a Σ calculation method for the simulated data.

Furthermore, the statistics of the number of grain boundary types can be found once the type of grain boundaries are quantified. For example, if high angle, low angle, $\Sigma 3$, $\Sigma 5$, $\Sigma 7$ or any other boundary types are found, the most common type of boundary can be determined, and the results can be validated with the experimental data. Some statistics that are used to describe the

fundamental mechanism governing the atomic movement in $\Sigma 5$ and $\Sigma 13$ are the quantitative string measurement, van Hove correlation function and the angular distribution function [39]. These or similar statistics will be used to quantify the correlated atomic movements for the boundary types calculated.

Finally, with the grain boundaries obtained, mobility studies will be performed in order to gain better understanding of the boundary motion characteristics. It is important to calculate the mobility of CdTe grain boundaries in order to predict grain structures. As grain boundaries affect solar cell efficiencies, study of the mobility of the boundaries will give the community a better understanding of this defect which will result in the development of better solar cells. The mobilities for $\Sigma 3$, $\Sigma 7$, and $\Sigma 11$ grain boundaries in CdTe have already been calculated by Aguirre et. al. [36]. The mobility for any other Σ value found in the polycrystalline structure can be calculated as well. Previously, these calculations were performed for very short-time scales (~ 1 ns). Simulations can be performed at long time scales (~ 10 ns) to capture the mobility of these grain boundaries better. For example, $\Sigma 3(311)$ grain boundary migration is not noticeable for the short-time scales simulation (0.9 ns) and therefore the long-time scale data is needed to derive a definitive mobility law for the $\Sigma 3(311)$ grain boundary migration.

5.2 TIMELINE

Figure 24 shows the tentative timeline for the research goals to be completed. The first four steps including; grain, boundary and amorphous atom identification along with grain orientation calculation are expected to be completed by summer 2019. Here, the most important step is to calculate the grain orientation which will be exported from GTA. However, if the GTA output cannot be properly interpreted, the orientation will be calculated manually by MATLAB with the

theoretical formulas. Then the main part of the proposed work i.e. quantifying the grain boundary types is scheduled to be completed within spring 2020. After the quantification, grain boundary characteristics analysis and the development of the new grain analysis tool should be completed by the end of summer 2020.

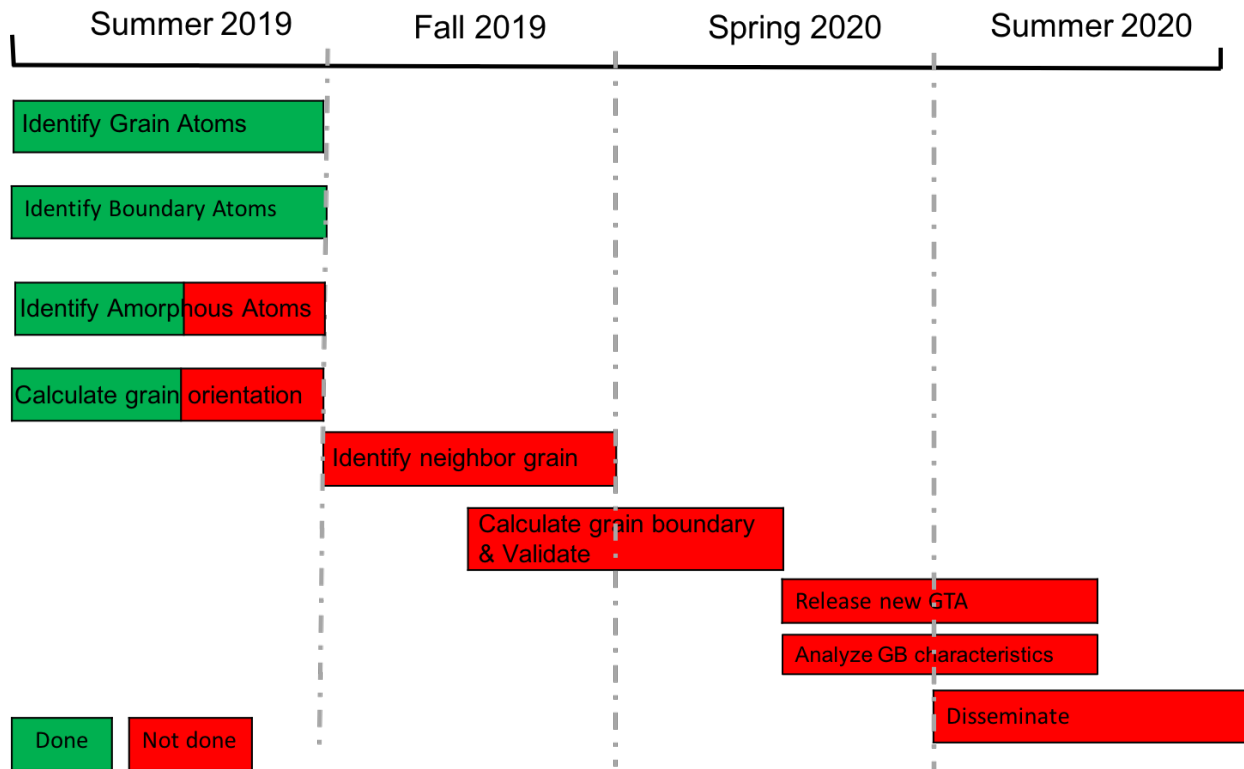


Figure 24. Timeline for the Proposed Work

References

- [1] Y. Yan and M. M. Al-Jassim, "Transmission electron microscopy of chalcogenide thin-film photovoltaic materials," *Curr. Opin. Solid State Mater. Sci.*, vol. 16, no. 1, pp. 39–44, 2012.
- [2] K. A. W. Horowitz *et al.*, "An analysis of the cost and performance of photovoltaic systems as a function of module area," *Natl. Renew. Energy Lab.*, vol. 1, no. 4, pp. 1–31, 2017.
- [3] R. W. Birkmire and E. Eser, "POLYCRYSTALLINE THIN FILM SOLAR CELLS: Present Status and Future Potential," *Annu. Rev. Mater. Sci.*, vol. 27, no. 1, pp. 625–653, 2002.
- [4] A. Balcioglu, R. K. Ahrenkiel, and F. Hasoon, "Deep-level impurities in CdTe/CdS thin-film solar cells," *J. Appl. Phys.*, vol. 88, no. 12, pp. 7175–7178, 2000.
- [5] J. Rangel-Cárdenas and H. Sobral, "Optical absorption enhancement in CdTe thin films by microstructuration of the silicon substrate," *Materials (Basel)*, vol. 10, no. 6, 2017.
- [6] W. Shockley and H. J. Queisser, "Detailed balance limit of efficiency of p-n junction solar cells," *J. Appl. Phys.*, vol. 32, no. 3, pp. 510–519, 1961.
- [7] NREL, "PV Research Cell Record Efficiency Chart." [Online]. Available: <https://www.nrel.gov/pv/assets/pdfs/pv-efficiency-chart.20181221.pdf>.
- [8] M. Gloeckler, I. Sankin, and Z. Zhao, "CdTe solar cells at the threshold to 20% efficiency," *IEEE J. Photovoltaics*, vol. 3, no. 4, pp. 1389–1393, 2013.
- [9] H. R. Moutinho *et al.*, "Grain boundary character and recombination properties in CdTe thin films," *Conf. Rec. IEEE Photovolt. Spec. Conf.*, pp. 3249–3254, 2013.
- [10] D. M. Jonathan, "Grain boundaries in CdTe thin film solar cells: a review," *Semicond. Sci. Technol.*, vol. 31, no. 9, p. 93001, 2016.
- [11] C. Li *et al.*, "From atomic structure to photovoltaic properties in CdTe solar cells," *Ultramicroscopy*, vol. 134, pp. 113–125, 2013.
- [12] M. M.K. and R. G. Forbes, "Atom probe tomography proteomics," vol. 60, no. 6, 2009.
- [13] B. J. Alder and T. E. Wainwright, "Studies in molecular dynamics. I. General method," *J. Chem. Phys.*, vol. 31, no. 2, pp. 459–466, 1959.
- [14] R. D.C., "Chemical Education Today The Art of Molecular Dynamics Simulation," vol. 76, no. 2, p. 44561, 1999.
- [15] R. Aguirre, J. J. Chavez, X. Zhou, and D. Zubia, "High Fidelity Polycrystalline CdTe/CdS Heterostructures via Molecular Dynamics," *MRS Adv.*, vol. 2, no. 53, pp. 3225–3230, 2017.
- [16] T. Xu and M. Li, "Topological and statistical properties of a constrained Voronoi tessellation," *Philosophical Magazine*, vol. 89, no. 4, pp. 349–374, 2009.
- [17] A. Stukowski and K. Albe, "Extracting dislocations and non-dislocation crystal defects from atomistic simulation data," *Model. Simul. Mater. Sci. Eng.*, vol. 18, no. 8, 2010.
- [18] G. J. Tucker and S. M. Foiles, "Quantifying the influence of twin boundaries on the deformation of nanocrystalline copper using atomistic simulations," *Int. J. Plast.*, vol. 65, no. 1989, pp. 191–205, 2015.
- [19] J. F. Panzarino and T. J. Rupert, "Tracking microstructure of crystalline materials: A post-processing algorithm for atomistic simulations," *Jom*, vol. 66, no. 3, pp. 417–428, 2014.
- [20] Porter, Easterling, and Sherif, *Phase Transformations in Metals and Alloys*, 3rd ed., vol. 3, no. 1. CRC Press, 2009.

- [21] G. Gottstein and Shvindlerman Lasar S., *Grain Boundary Migration in Metals: Thermodynamics, Kinetics, Applications, Second Edition*, 2nd ed. CRC Press.
- [22] G. Stechmann *et al.*, “3-Dimensional microstructural characterization of CdTe absorber layers from CdTe / CdS thin film solar cells,” *Sol. Energy Mater. Sol. Cells*, vol. 151, pp. 66–80, 2016.
- [23] W. K. Metzger *et al.*, “Recombination by grain-boundary type in CdTe,” *J. Appl. Phys.*, vol. 118, no. 2, p. 025702, 2015.
- [24] V. Consonni, N. Baier, O. Robach, C. Cayron, F. Donatini, and G. Feuillet, “Local band bending and grain-to-grain interaction induced strain nonuniformity in polycrystalline CdTe films,” *Phys. Rev. B - Condens. Matter Mater. Phys.*, vol. 89, no. 3, pp. 1–10, 2014.
- [25] M. M. Nowell, M. A. Scarpulla, N. R. Paudel, K. A. Wieland, A. D. Compaan, and X. Liu, “Characterization of Sputtered CdTe Thin Films with Electron Backscatter Diffraction and Correlation with Device Performance,” *Microsc. Microanal.*, vol. 21, no. 4, pp. 927–935, 2015.
- [26] D. G. Pettifor and I. I. Oleinik, “Analytic bond-order potentials beyond tersoff-brenner. i. theory,” *Phys. Rev. B - Condens. Matter Mater. Phys.*, vol. 59, no. 13, pp. 8487–8499, 1999.
- [27] J.E. Jones, “On the Determination of Molecular Fields.-II. From the Equation of State of a Gas,” vol. 4, no. 71, 1924.
- [28] F. H. Stillinger and T. A. Weber, “Computer simulation of local order in condensed phases of silicon,” *Phys. Rev. B*, vol. 31, no. 8, pp. 5262–5271, 1985.
- [29] X. W. Zhou, D. K. Ward, J. E. Martin, F. B. Van Swol, J. L. Cruz-Campa, and D. Zubia, “Stillinger-Weber potential for the II-VI elements Zn-Cd-Hg-S-Se-Te,” *Phys. Rev. B - Condens. Matter Mater. Phys.*, vol. 88, no. 8, pp. 1–14, 2013.
- [30] F. Ercolessi, “Dipartimento di Scienze Matematiche, Informatiche e Fisiche. Univesita degli Studi di Udine, [Online],” 2017.
- [31] A. I. Motion, *Atoms In Motion - Chapter 5 - MD Molecular Dynamics (MD) A Few Notes on the Atomistic Simulations*. 2017.
- [32] R. Aguirre *et al.*, “Crystal Growth and Atom Diffusion in (Cu)ZnTe/CdTe via Molecular Dynamics,” *IEEE J. Photovoltaics*, vol. 8, no. 2, pp. 594–599, 2018.
- [33] J. J. Chavez, X. W. Zhou, S. F. Almeida, R. Aguirre, and D. Zubia, “Molecular Dynamics Simulations of CdTe / CdS Heteroepitaxy - Effect of Substrate Orientation,” *J. Mater. Sci. Res.*, vol. 5, no. 3, p. 1, 2016.
- [34] S. Plimpton, “Plimpton1995.Pdf,” *Journal of Computational Physics*, vol. 117, no. 1. pp. 1–19, 1995.
- [35] K. G. F. Janssens, D. Olmsted, E. A. Holm, S. M. Foiles, S. J. Plimpton, and P. M. Derlet, “Computing the mobility of grain boundaries,” *Nat. Mater.*, vol. 5, no. 2, pp. 124–127, 2006.
- [36] R. Aguirre, S. Abdullah, X. Zhou, and D. Zubia, “Molecular Dynamics Calculations of Grain Boundary Mobility in CdTe,” *Nanomaterials*, vol. 9, no. 4, p. 552, 2019.
- [37] A. Stukowski, “Structure identification methods for atomistic simulations of crystalline materials,” *Model. Simul. Mater. Sci. Eng.*, vol. 20, no. 4, 2012.
- [38] H. Ibach and H. Luth, *Solid-State Physics*, 4th ed. Springer-Verlag Berlin, 2009.
- [39] X. Yan and H. Zhang, “On the atomistic mechanisms of grain boundary migration in [0 0 1] twist boundaries: Molecular dynamics simulations,” *Comput. Mater. Sci.*, vol. 48, no. 4, pp. 773–782, 2010.

Appendices

APPENDIX A- INPUT FILE FOR CREATING $\Sigma 3(111)$ USING LAMMPS CODE

```
&maincard
ntypes=7
perub={3.0*nx*alat/sqrt(6.0)-0.5},{6.0*ny*alat/sqrt(3.0)-
0.5*alat/sqrt(3.0)},{2.0*nz*alat/sqrt(2.0)-0.5}
perl=-0.5,{0.0-0.5*alat/sqrt(3.0)},{-0.5
ilatseed={ilatseed}
amass=112.41,127.60,112.41,127.60,112.41,127.60,112.41
ielement=48,52,48,52,48,52,48
iseed=212121
&end

&latcard
lattice='fcc'
alat={alat},{alat},{alat}
xrot=1.0,1.0,-2.0
yrot=1.0,1.0,1.0
zrot=1.0,-1.0,0.0
ybound={3.0*ny*alat/sqrt(3.0)-0.5*alat/sqrt(3.0)},{6.0*ny*alat/sqrt(3.0)-
0.5*alat/sqrt(3.0)}
periodicity=3.0,3.0,2.0
strain=0.0,0.0,0.0
delx=0.0,0.0,0.0
uvw=1.0,1.0,1.0
omega=60.0
delx={0.0-sqrt(6.0)*alat/12.0},0.0,{0.0-sqrt(2.0)*alat/4.0}
&end
&subcard
rcell=0.0,0.0,0.0
ccell=1.0,0.0,0.0,0.0,0.0,0.0,0.0,0.0
&end
&subcard
rcell=0.25,0.25,0.25
ccell=0.0,1.0,0.0,0.0,0.0,0.0,0.0,0.0
&end
&subcard
&end
&defcard
&end
&latcard
lattice='fcc'
alat={alat},{alat},{alat}
xrot=1.0,1.0,-2.0
yrot=1.0,1.0,1.0
```

```

zrot=1.0,-1.0,0.0
ybound={0.0-0.5*alat/sqrt(3.0)},{3.0*ny*alat/sqrt(3.0)-0.5*alat/sqrt(3.0)}
periodicity=3.0,3.0,2.0
strain=0.0,0.0,0.0
delx=0.0,0.0,0.0
&end
&subcard
rcell=0.0,0.0,0.0
ccell=0.0,0.0,1.0,0.0,0.0,0.0,0.0
&end
&subcard
rcell=0.25,0.25,0.25
ccell=0.0,0.0,0.0,1.0,0.0,0.0,0.0
&end
&subcard
&end
&defcard
&end
&latcard
lattice='fcc'
alat={alat},{alat},{alat}
xrot=1.0,1.0,-2.0
yrot=1.0,1.0,1.0
zrot=1.0,-1.0,0.0
ybound={3.0*ny*alat/sqrt(3.0)-0.5*alat/sqrt(3.0)},{6.0*ny*alat/sqrt(3.0)-
0.5*alat/sqrt(3.0)}
periodicity=3.0,3.0,2.0
strain=0.0,0.0,0.0
delx=0.0,0.0,0.0
sigma='yes'
&end
&subcard
rcell=0.0,0.0,0.0
ccell=0.0,0.0,0.0,0.0,0.0,1.0,0.0
&end
&subcard
rcell=0.25,0.25,0.25
ccell=0.0,0.0,0.0,0.0,0.0,0.0,1.0
&end
&subcard
&end
&defcard
style='box'
oldtype=6
newtype=-1
prob=1.0

```

```

&end
&defcard
  style='box'
  oldtype=7
  newtype=-2
  prob=1.0
&end
&defcard
&end
&latcard
&end

&rotatecard
&end

&hitcard
&end

&disturbcard
  dismax=0.0
  strain=0.0,0.0,0.0
&end

&shiftcard
  mode=4
  deltax=0.0
  deltax=0.0
  deltaz=0.0
&end

&velcard
&end

&filecard
  dynamo="none"
  paradyn="none"
  lammmps="{inputfile}"
  xyz="none"
  ensight="{ensight}"
&end

```

APPENDIX B- INPUT FILE FOR CREATING $\Sigma 7(111)$

```
&maincard
ntypes=7
perub={14.0*nx*alat/sqrt(14.0)-0.5},{6.0*ny*alat/sqrt(3.0)-
0.5},{42.0*nz*alat/sqrt(42.0)-0.5}
perlbb=-0.5,-0.5,-0.5
ilatseed={ilatseed}
amass=112.41,127.60,112.41,127.60,112.41,127.60,112.41
ielement=48,52,48,52,48,52,48
iseed=212121
&end

&latcard
lattype='fcc'
alat={alat},{alat},{alat}
xrot=2.0,1.0,-3.0
yrot=1.0,1.0,1.0
zrot=4.0,-5.0,1.0
periodicity=14.0,3.0,42.0
strain=0.0,0.0,0.0
delx=0.0,0.0,0.0
uvw=1.0,1.0,1.0
omega=-38.2132107
ybound={3.0*ny*alat/sqrt(3.0)-0.5},{6.0*ny*alat/sqrt(3.0)-0.5}
&end
&subcard
rcell=0.0,0.0,0.0
ccell=1.0,0.0,0.0,0.0,0.0,0.0,0.0,0.0
&end
&subcard
rcell=0.25,0.25,0.25
ccell=0.0,1.0,0.0,0.0,0.0,0.0,0.0,0.0
&end
&subcard
&end
&defcard
&end
&latcard
lattype='fcc'
alat={alat},{alat},{alat}
xrot=2.0,1.0,-3.0
yrot=1.0,1.0,1.0
zrot=4.0,-5.0,1.0
periodicity=14.0,3.0,42.0
strain=0.0,0.0,0.0
delx=0.0,0.0,0.0
```

```

ybound=-0.5,{3.0*ny*alat/sqrt(3.0)-0.5}
&end
&subcard
rcell=0.0,0.0,0.0
ccell=0.0,0.0,1.0,0.0,0.0,0.0,0.0
&end
&subcard
rcell=0.25,0.25,0.25
ccell=0.0,0.0,0.0,1.0,0.0,0.0,0.0
&end
&subcard
&end
&defcard
&end
&latcard
lattype='fcc'
alat={alat},{alat},{alat}
xrot=2.0,1.0,-3.0
yrot=1.0,1.0,1.0
zrot=4.0,-5.0,1.0
periodicity=14.0,3.0,42.0
strain=0.0,0.0,0.0
delx=0.0,0.0,0.0
ybound={3.0*ny*alat/sqrt(3.0)-0.5},{6.0*ny*alat/sqrt(3.0)-0.5}
sigma='yes'
&end
&subcard
rcell=0.0,0.0,0.0
ccell=0.0,0.0,0.0,0.0,0.0,1.0,0.0
&end
&subcard
rcell=0.25,0.25,0.25
ccell=0.0,0.0,0.0,0.0,0.0,0.0,1.0
&end
&subcard
&end
&defcard
style='box'
oldtype=6
newtype=-1
prob=1.0
&end
&defcard
style='box'
oldtype=7
newtype=-2

```



```

    prob=1.0
    &end
    &defcard
    &end
    &latcard
    &end

    &rotatecard
    &end

    &hitcard
    &end

    &disturbcard
    dismax=0.0
    strain=0.0,0.0,0.0
    &end

    &shiftcard
    mode=4
    deltax=0.0
    deltay=0.0
    deltaz=0.0
    &end

    &velcard
    &end

    &filecard
    dynamo="none"
    paradyn="none"
    lammmps="{inputfile}"
    xyz="none"
    ensight="{ensight}"
&end

```

APPENDIX C- INPUT FILE FOR CREATING $\Sigma 11(311)$

```

    &maincard
    ntypes=7
    perub={2.0*nx*alat/sqrt(2.0)-0.5},{22.0*ny*alat/sqrt(11.0)-
0.5},{22.0*nz*alat/sqrt(22.0)-0.5}
    perl=-0.5,-0.5,-0.5
    ilatseed={ilatseed}
    amass=112.41,127.60,112.41,127.60,112.41,127.60,112.41
    ielement=48,52,48,52,48,52,48
    iseed=212121

```

```

&end

&latcard
lattice='fcc'
alat={alat},{alat},{alat}
xrot=0.0,-1.0,1.0
yrot=3.0,1.0,1.0
zrot=-2.0,3.0,3.0
periodicity=2.0,11.0,22.0
strain=0.0,0.0,0.0
delx=0.0,0.0,0.0
uvw=0.0,-1.0,1.0
omega=-50.4788036
ybound={11.0*ny*alat/sqrt(11.0)-0.5},{22.0*ny*alat/sqrt(11.0)-0.5}
&end
&subcard
rcell=0.0,0.0,0.0
ccell=1.0,0.0,0.0,0.0,0.0,0.0,0.0,0.0
&end
&subcard
rcell=0.25,0.25,0.25
ccell=0.0,1.0,0.0,0.0,0.0,0.0,0.0,0.0
&end
&subcard
&end
&defcard
&end
&latcard
lattice='fcc'
alat={alat},{alat},{alat}
xrot=0.0,-1.0,1.0
yrot=3.0,1.0,1.0
zrot=-2.0,3.0,3.0
periodicity=2.0,11.0,22.0
strain=0.0,0.0,0.0
delx=0.0,0.0,0.0
ybound=-0.5,{11.0*ny*alat/sqrt(11.0)-0.5}
&end
&subcard
rcell=0.0,0.0,0.0
ccell=0.0,0.0,1.0,0.0,0.0,0.0,0.0,0.0
&end
&subcard
rcell=0.25,0.25,0.25
ccell=0.0,0.0,0.0,1.0,0.0,0.0,0.0,0.0
&end

```

```

&subcard
&end
&defcard
&end
&latcard
lattice='fcc'
alat={alat},{alat},{alat}
xrot=0.0,-1.0,1.0
yrot=3.0,1.0,1.0
zrot=-2.0,3.0,3.0
periodicity=2.0,11.0,22.0
strain=0.0,0.0,0.0
delx=0.0,0.0,0.0
ybound={11.0*ny*alat/sqrt(11.0)-0.5},{22.0*ny*alat/sqrt(11.0)-0.5}
sigma='yes'
&end
&subcard
rcell=0.0,0.0,0.0
ccell=0.0,0.0,0.0,0.0,0.0,1.0,0.0
&end
&subcard
rcell=0.25,0.25,0.25
ccell=0.0,0.0,0.0,0.0,0.0,0.0,1.0
&end
&subcard
&end
&defcard
style='box'
oldtype=6
newtype=-1
prob=1.0
&end
&defcard
style='box'
oldtype=7
newtype=-2
prob=1.0
&end
&defcard
&end
&latcard
&end

&rotatecard
&end

```

```

&hitcard
&end

&disturbcard
dismax=0.0
strain=0.0,0.0,0.0
&end

&shiftcard
mode=4
deltax=0.0
deltay=0.0
deltaz=0.0
&end

&velcard
&end

&filecard
dynamo="none"
paradyn="none"
lammmps="{inputfile}"
xyz="{ensight}"
ensight="{ensight}"
&end

```

APPENDIX D- CODE FOR EXECUTING $\Sigma 7(111)$ BOUNDARY MIGRATION

```

#!/bin/bash
#-----
# SLURM resource manager settings
#-----
#SBATCH -J Sigma7    # Job name
#SBATCH -o Sigma7.o%j # Name of stdout output file(%j expands to jobId)
#SBATCH -e Sigma7.o%j # Name of stderr output file(%j expands to jobId)
#SBATCH -p compute    # Submit to the 'normal' or 'development' queue
#SBATCH -N 1           # Total number of nodes requested (16 cores/node)
#SBATCH -n 16          # Total number of mpi tasks requested
#SBATCH -t 04:00:00    # Run time (hh:mm:ss)
# development queue max running hours: 2 hours
# normal    queue max running hours: 48 hours
# gpu       queue max running hours: 24 hours
# gpudev    queue max running hours: 4 hours
# The next line is required if the user has more than one project

```

```

#SBATCH -A TG-DMR150105    # Allocation name to charge job against
#-----
# clean old files
#-----
/bin/rm -rf stdout log.lammps r.* restart.* test_*
#-----
# load stampede modules needed for lammps operation
#-----
module load openkim/1.2.2
module load voro++/0.4.5
module load xalt/0.6
#-----
# directory path configuration
#-----
my_dir=$HOME/setup # base dir
lmp=$my_dir/executables/lmp_comet # lammps executable
#pot=potentials/AlCu.set      # EAM potential
pot=$my_dir/potential/CdTeZnSeHgSCu2.sw # SW potential file
ai=$my_dir/templates/a_xiaowang2_withAnneal.i # lammps input template file
exec=$my_dir/executables # executable dir
#-----
# lammps simulation modifiers
#-----
nodes=1 # nodes
cores=16 # cores
npx=4 # number of cores in x axis for lammps box
npz=4 # number of cores in z axis for lammps box
temp=1800.0 # target isothermal temperature
totn=100 # number of time steps in simulation
noutput=1 # number of time steps to print output file
#-----
# substrate modifiers
#-----
alatZB=6.478 # CdS z.b. lattice parameter

#-----
# create initial lammps input file
#-----
$exec/ipp alatZB=$alatZB temp=$temp noutput=$noutput totn=$totn npz=$npz
pot=$pot $ai > a.i
#-----
# submit job to queue
#-----
ibrun -o 0 -n $(( $nodes*$cores )) $lmp < a.i >& stdout

```

APPENDIX E- MODIFIED MATLAB CODE TO RUN GTA TOOL

To execute the GTA tool in MatLab 2016, the code (GRAIN_TRACKING_ALGORITHM.m script, line number 638) of Panzarino et al [19] was modified as highlighted.

```
%%TypeofPlots == 4 from Main Original Code
function pushbutton6_callback(hObject,eventdata)
    prompt = 'Choose a simulation direction to inversely project orientation
normals stereographically: Use the format: [a b c]';
    dlg_title = 'Orientation Mapping';
    num_lines = 1;
    def = {' '};
    answer = inputdlg(prompt,dlg_title,num_lines,def);
    Axis = str2num(answer{1});

    try
        h5 = msgbox('Running!');
        [Orientation_Matrix] =
InversePole(Axis,Crystal_Axis_No_Mapping,filenum);
        delete(h5);

    catch
        delete(h5);
        error('Please Load Data from Grain Visualization');
    end
    [Orientation_Matrix] =
Crystal_Symmetry_For_Orientation_Map(Orientation_Matrix,filenum);

    for k = 1:filenum %added the plus 10 for figure printing. conflicted with
main figure GUI
        OrientationMap(A_Matrix,Orientation_Matrix,k) %added +10 to this
function
    end

    % figure(gcf+1) %Generate new figure
    figure(get(gcf,'Number')+1)
    image(imread('Key.png')) %Plot The Key on this Figure
    % GenerateOrientationKey(k + 11) %Manual Generation of Key Triangle
    % (higher Quality, longer run time)

    msgbox('Visualization Complete!');
end
```

Vita

Sharmin Abdullah was born in Dhaka, Bangladesh. She got her secondary and higher secondary school certificates in 2006 and 2008 respectively from Viqarunnisa Noon School and College in Dhaka, Bangladesh. She started her bachelor's degree in Electrical and Electronic Engineering from Ahsanullah University of Science and Technology, Bangladesh in following year. She received Dean's honor list award for academic excellence and graduated in 2012.

After pursuing her bachelor's degree, she started working as a laboratory instructor in the Electrical and Computer Engineering department of North South University in Dhaka, Bangladesh. She got accepted with a teaching assistantship in the Computational Science program at University of Texas at El Paso (UTEP) to pursue her Doctoral degree in fall 2016. Currently, she is working as a research assistant at Nanomil Lab in the Electrical and Computer Engineering Department of UTEP.

Sharmin's research focus is on atomistic simulations of material characteristics. She is working on analyzing the microstructures of photovoltaic thin film materials to improve the solar cell efficiency and making it cost effective. She has performed research for a project funded by the U.S. Department of Energy and collaborated with the scientist from Sandia National Laboratories. She has attended several national and international research conferences.

Email address: sabdullah@miners.utep.edu

This thesis was typed by Sharmin Abdullah.